BOSTON UNIVERSITY

GRADUATE SCHOOL OF ARTS AND SCIENCES

Dissertation

STATISTICAL PHYSICS APPROACHES TO UNDERSTAND

PHYSIOLOGICAL SIGNALS

by

ZHI CHEN

B.S., University of Science and Technology of China, 1995
Master, University of Science and Technology of China, 1998

Submitted in partial fulfillment of the

requirements for the degree of

Doctor of Philosophy

2004

Approved by

First Reader ————————————————————————
H. Eugene Stanley, Ph.D.
University Professor,
Professor of Physics

Second Reader ————————————————————————
William J. Skocpol, Ph.D.
Professor of Physics

Contents

List of Tables

List of Figures

List of Abbreviations

DFA   detrended fluctuation analy

BFV   blood flow velo

MCA   middle cerebral art

BP   blood press

Part I

Introduction

Part II

Effects of Trends and Nonstationarities

Chapter 1

Effect of Trends on Detrended Fluctuation Analysis

1.1 Overview

Detrended fluctuation analysis (DFA) is a scaling analysis method used to estimate long-range power-law correlation exponents in noisy signals. Many noisy signals in real systems display trends, so that the scaling results obtained from the DFA method become difficult to analyze. We systematically study the effects of three types of trends — linear, periodic, and power-law trends, and offer examples where these trends are likely to occur in real data. We compare the difference between the scaling results for artificially generated correlated noise and correlated noise with a trend, and study how trends lead to the appearance of crossovers in the scaling behavior. We find that crossovers result from the competition between the scaling of the noise and the "apparent" scaling of the trend. We study how the characteristics of these crossovers depend on (i) the slope of the linear trend; (ii) the amplitude and period of the periodic trend; (iii) the amplitude and power of the power-law trend and (iv) the length as well as the correlation properties of the noise. Surprisingly, we find that the crossovers in the scaling of noisy signals with trends also follow scaling laws — i.e. long-range power-law dependence of the position of the crossover on the parameters of the trends. We show that the DFA result of noise with a trend can be exactly determined by

the superposition of the separate results of the DFA on the noise and on the trend, assuming that the noise and the trend are not correlated. If this superposition rule is not followed, this is an indication that the noise and the superimposed trend are not independent, so that removing the trend could lead to changes in the correlation properties of the noise. In addition, we show how to use DFA appropriately to minimize the effects of trends, and how to recognize if a crossover indicates indeed a transition from one type to a different type of underlying correlation, or the crossover is due to a trend without any transition in the dynamical properties of the noise.

1.2 Introduction to this chapter

Many physical and biological systems exhibit complex behavior characterized by long-range power-law correlations. Traditional approaches such as the power-spectrum and correlation analysis are not suited to accurately quantify long-range correlations in non-stationary signals — e.g. signals exhibiting fluctuations along polynomial trends. Detrended fluctuation analysis (DFA) [1–4] is a scaling analysis method providing a simple quantitative parameter — the scaling exponent α — to represent the correlation properties of a signal. The advantages of DFA over many methods are that it permits the detection of long-range correlations embedded in seemingly non-stationary time series, and also avoids the spurious detection of apparent long-range correlations that are artifact of non-stationarity. In the past few years more than 100 publications have utilized the DFA as method of correlation analysis, and have uncovered long-range power-law correlations in many research fields such as cardiac dynamics [5–23], bioinformatics [1, 2, 24–34], economics [35–47], meteorology [48–50], geology [51], ethology [52] etc. Furthermore, the DFA method may help identify different states of the same system according to its different scaling behaviors — e.g. the scaling exponent α for heart inter-beat intervals is different for healthy and sick individuals [14, 16, 17, 53].

The correct interpretation of the scaling results obtained by the DFA method is crucial for understanding the intrinsic dynamics of the systems under study. In fact, for all systems where the DFA method was applied, there are many issues that remain unexplained. One

the common challenges is that the correlation exponent is not always a constant (independent of scale) and crossovers often exist — i.e. change of the scaling exponent α for different range of scales [5, 16, 35]. A crossover usually can arise from a change in the correlation properties of the signal at different time or space scales, or can often arise from trends in the data. In this paper, we systematically study how different types of trends affect the apparent scaling behavior of long-range correlated signals. The existence of trends in times series generated by physical or biological systems is so common that it is almost unavoidable. For example, the number of particles emitted by a radiation source in an unit time has a trend of decreasing because the source becomes weaker [54, 55]; the density of air due to gravity has a trend at different altitude [56]; the air temperature in different geographic locations and the water flow of rivers have a periodic trend due to seasonal changes [49, 50, 57–59]; the occurrence rate of earthquakes in certain area has trend in different time period [60].

An immediate problem facing researchers applying scaling analysis to time series is whether trends in data arise from external conditions, having little to do with the intrinsic dynamics of the system generating noisy fluctuating data. In this case, a possible approach is to first recognize and filter out the trends before we attempt to quantify correlations in the noise. Alternatively, trends may arise from the intrinsic dynamics of the system, rather than being an epiphenomenon of external conditions, and thus may be correlated with the noisy fluctuations generated by the system. In this case, careful considerations should be given if trends should be filtered out when estimating correlations in the noise, since such "intrinsic" trends may be related to the local properties of the noisy fluctuations.

Here we study the origin and the properties of crossovers in the scaling behavior of noisy signals, by applying the DFA method first on correlated noise and then on noise with trends, and comparing the difference in the scaling results. To this end, we generate artificial time series — anticorrelated, white and correlated noise with standard deviation equal to one — using the modified Fourier filtering method introduced by Makse et al. [61]. We consider the case when the trend is independent of the local properties of the noise (external trend). We find that the scaling behavior of noise with a trend is a superposition of the scaling of

the noise and the apparent scaling of the trend, and we derive analytical relations based on the DFA, which we call "superposition rule". We show how this "superposition rule" can be used to determine if the trends are independent of the noisy fluctuation in real data, and if filtering these trends out will no affect the scaling properties of the data.

The outline of this section is as follows. In Sec.1.3, we review the algorithm of the DFA method, In Sec. 1.4, we consider the effect of a linear trend. In Sec. 1.5, we study a periodic trend, and in Sec. 1.6 the effect of power-law trend. We systematically study all resulting crossovers, their conditions of existence and their typical characteristics associated with the different types of trends. Further, we discuss some general rules regarding the effect of trends in Sec. 1.7. Finally, Sec. 1.8 contains a summary.

1.3   Detrended Fluctuation Analysis (DFA) Method

Using a modified Fourier filtering method [61], we can generate stationary uncorrelated, correlated, and anti-correlated signals $u(k)$ ($k = 1, 2, 3, ..., N_{\max}$) with a standard deviation $\sigma = 1$. This method consists of the following steps:

(a) First, we generate an uncorrelated and Gaussian distributed sequence $\eta(k)$ and calculate the Fourier transform coefficients $\eta(q)$.

(b) The desired signal $u(k)$ must exhibit correlations, which are defined by the form of the power spectrum

$$S(q) = \langle u(q)u(-q)\rangle \sim q^{-(1-\gamma)},$$

where $u(q)$ are the Fourier transform coefficients of $u(k)$ and γ is the correlation exponent. Thus, we generate $u(q)$ using the following transformation:

$$u(q) = [S(q)]^{1/2}\eta(q),$$

where $S(q)$ is the desired power spectrum in Eq. (1.1).

(c) We calculate the inverse Fourier transform of $u(q)$ to obtain $u(k)$.

Next, we briefly introduce the DFA method, which involves the following steps [1]:
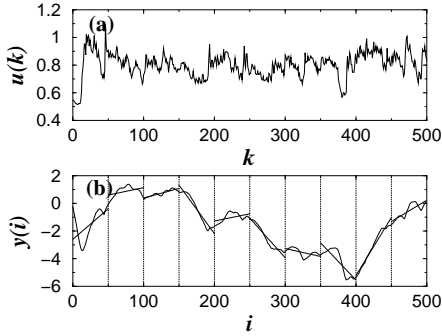
Figure 1.1: Algorithm of DFA method.

(a) The correlated signal $u(k)$. (b) The integrated signal: $y(i) = \sum_{k=1}^{i}[u(k) - \langle u \rangle]$. The vertical dotted lines indicate a box of size $n = 100$, the solid straight lines segments are the estimated linear "trend" in each box by least-squares fit.

(i) Starting with a correlated signal $u(k)$, where $k = 1, .., N_{max}$ and N_{max} is the length of the signal, we first integrate the signal $u(k)$ and obtain $y(i) \equiv \sum_{k=1}^{i}[u(k) - \langle u \rangle]$, where $\langle u \rangle$ is the mean.

(ii) The integrated signal $y(i)$ is divided into boxes of equal length n.

(iii) In each box of length n, we fit $y(i)$, using a polynomial function of order ℓ which represents the *trend* in that box. The y coordinate of the fit line in each box is denoted by $y_n(i)$ (see Fig. 1.1, where linear fit is used). Since we use a polynomial fit of order ℓ, we denote the algorithm as DFA-ℓ.

(iv) The integrated signal $y(i)$ is detrended by subtracting the local trend $y_n(i)$ in each box of length n.

(v) For a given box size n, the root mean-square (r.m.s.) fluctuation for this integrated and detrended signal is calculated:

$$F(n) \equiv \sqrt{\frac{1}{N_{max}} \sum_{i=1}^{N_{max}} [Y(i)]^2}, \tag{1.3}$$

where

$$Y(i) = y(i) - y_n(i), \tag{}$$

is called detrended fluctuation function.

(vi) The above computation is repeated for a broad range of scales (box sizes n) provide a relationship between $F(n)$ and the box size n.

A power-law relation between the average root-mean-square fluctuation function F and the box size n indicates the presence of scaling: $F(n) \sim n^{\alpha}$. The fluctuations be characterized by a scaling exponent α, a self-similarity parameter which represents long-range power-law correlation properties of the signal. If $\alpha = 0.5$, there is no correlat and the signal is uncorrelated (white noise); if $\alpha < 0.5$, the signal is anti-correlated $\alpha > 0.5$, the signal is correlated (We note that when $0 < \gamma < 1$, α and γ have the follow relation: $\alpha = (2 - \gamma)/2$).

1.4 Noise with linear trends

First we consider the simplest case: correlated noise with a linear trend. A linear trend

$$u(i) = A_{\mathrm{L}}i \tag{}$$

is characterized by only one variable — the slope of the trend, A_{L}. For convenience, denote the r.m.s. fluctuation function for noise without trends by $F_{\eta}(n)$, linear trends $F_{\mathrm{L}}(n)$, and noise with a linear trend by $F_{\eta \mathrm{L}}(n)$.

1.4.1 DFA-1 on noise with a linear trend

Using the algorithm of Makse [61], we generate correlated noise with standard deviat one, with a given correlation property characterized by a given scaling exponent α. apply DFA-1 to quantify the correlation properties of the noise and find that only in cert good fit region the r.m.s. fluctuation function $F_{\eta}(n)$ can be approximated by a power-function [62].

$$F_\eta(n) = b_0 n^\alpha \tag{1.6}$$

where b_0 is a parameter independent of the scale n. We also derive analytically the r.m.s. fluctuation function for linear trend only for DFA-1 and find that [62]

$$F_L(n) = k_0 A_L n^{\alpha_L} \tag{1.7}$$

where k_0 is a constant independent of the length of trend N_{max}, of the box size n and of the slope of the trend A_L. We obtain $\alpha_L = 2$.
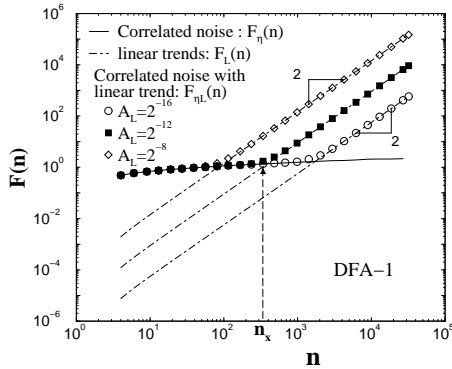
Figure 1.2: Crossover behavior of the r.m.s. fluctuation function for noise with superposed linear trends.
The length of the noise (with correlation exponent $\alpha = 0.1$) is $N_{max} = 2^{17}$, and the slopes of superposed linear trends are $A_L = 2^{-16}, 2^{-12}, 2^{-8}$. For comparison, we show $F_\eta(n)$ for the noise (thick solid line) and $F_L(n)$ for the linear trends (dot-dashed line) (Eq.(1.7)). The results show that a crossover at a scale $n_\times$ for $F_{\eta L}(n)$. For $n < n_\times$, the noise dominates and $F_{\eta L}(n) \approx F_\eta(n)$. For $n > n_\times$, the linear trend dominates and $F_{\eta L}(n) \approx F_L(n)$.

Next we apply the DFA-1 method to the superposition of a linear trend with correlated noise and we compare the r.m.s. fluctuation function $F_{\eta L}(n)$ with $F_\eta(n)$ [see Fig.1.2]. We observe a crossover in $F_{\eta L}(n)$ at scale $n = n_\times$. For $n < n_\times$, the behavior of $F_{\eta L}(n)$ is

very close to the behavior of $F_\eta(n)$, while for $n > n_\times$, the behavior of $F_{\eta L}(n)$ is very close to the behavior of $F_L(n)$. A similar crossover behavior is also observed in the scaling of the well-studied biased random walk [63, 64]. It is known that the crossover in the biased random walk is due to the competition of the unbiased random walk and the bias [see Fig. of [64]]. We illustrate this observation in Fig. 1.3, where the detrended fluctuation function (Eq. (1.4)) of the correlated noise, $Y_\eta(i)$, and of the noise with a linear trend, $Y_{\eta L}(i)$ are shown. For the box size $n < n_\times$ as shown in Fig. 1.3(a) and (b), $Y_{\eta L}(i) \approx Y_\eta(i)$. For $n > n_\times$ as shown in Fig. 1.3(c) and (d), $Y_{\eta L}(i)$ has distinguishable quadratic background significantly different from $Y_\eta(i)$. This quadratic background is due to the integration of the linear trend within the DFA procedure and represents the detrended fluctuation function Y_L of the linear trend. These relations between the detrended fluctuation functions $Y(i)$ at different time scales n explain the crossover in the scaling behavior of $F_{\eta L}(n)$: from very close to $F_\eta(n)$ to very close to $F_L(n)$ (observed in Fig.1.2).

The experimental results presented in Figs.1.2 and 1.3 suggest that the r.m.s. fluctuation function for a signal which is a superposition of a correlated noise and a linear trend can be expressed as:

$$[F_{\eta L}(n)]^2 = [F_L(n)]^2 + [F_\eta(n)]^2 \tag{1.8}$$

We provide an analytic derivation of this relation in 1.7.1, where we show that Eq.(1.8) holds for the superposition of any two independent signals — in this particular case noise and linear trend. We call this relation the "superposition rule". This rule helps us understand how the competition between the contribution of the noise and the trend to the r.m.s. fluctuation function $F_{\eta L}(n)$ at different scales n leads to appearance of crossovers [63].

Next, we ask how the crossover scale $n_\times$ depends on: (i) the slope of the linear trend A_L, (ii) the scaling exponent α of the noise, and (iii) the length of the signal N_{max}. Surprisingly, we find that for noise with any given correlation exponent α the crossover scale $n_\times$ itself follows a power-law scaling relation over several decades: $n_\times \sim (A_L)^\theta$ (see Fig. 1.4). We find that in this scaling relation, the crossover exponent θ is negative and its value depends on the correlation exponent α of the noise — the magnitude of θ decreases when α increases.
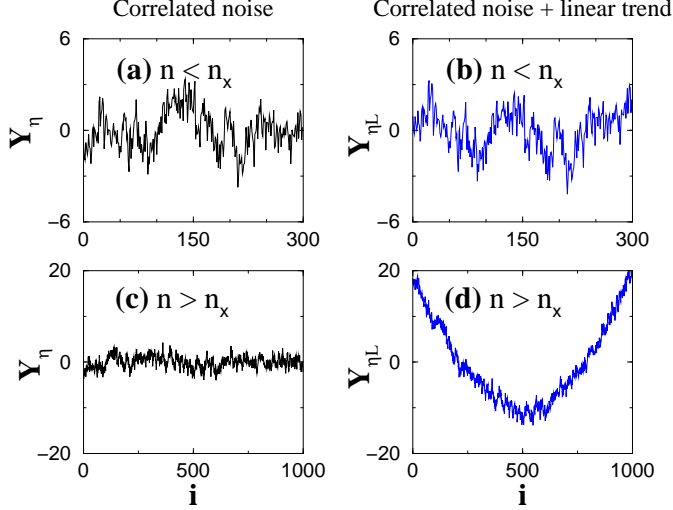
Figure 1.3: Comparison of the detrended fluctuation function for noise $Y_\eta(i)$ and for noise with linear trend $Y_{\eta L}(i)$ at different scales.

(a) and (c) are Y_η for noise with $\alpha = 0.1$; (b) and (d) are $Y_{\eta L}$ for the same noise with a linear trend with slope $A_L = 2^{-12}$ (the crossover scale $n_\times = 320$ see Fig. 1.2). (a) (b) for scales $n < n_\times$ the effect of the trend is not pronounced and $Y_\eta \approx Y_{\eta L}$ (i.e. $Y_\eta \gg Y_L$); (c)(d) for scales $n > n_\times$, the linear trend is dominant and $Y_\eta \ll Y_{\eta L}$.

We present the values of the "crossover exponent" θ for different correlation exponents α in Table 1.1.

To understand how the crossover scale depends on the correlation exponent α of the noise we employ the superposition rule [Eq.(1.8)] and estimate $n_\times$ as the intercept between $F_\eta(n)$ and $F_L(n)$. From the Eqs. (1.6) and (1.7), we obtain the following dependence of $n_\times$ on α:

$$n_\times = \left(A_L \frac{k_0}{b_0}\right)^{1/(\alpha - \alpha_L)} = \left(A_L \frac{k_0}{b_0}\right)^{1/(\alpha - 2)} \tag{1.9}$$

This analytical calculation for the crossover exponent $-1/(\alpha_L - \alpha)$ is in a good agreement
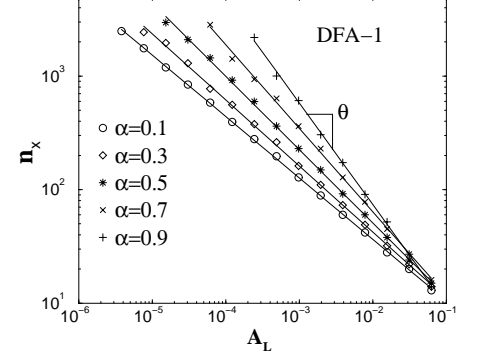
Figure 1.4: The crossover $n_\times$ of $F_{\eta L}(n)$ for different noises with a linear trend. We determine the crossover scale $n_\times$ based on the difference Δ between $\log F_\eta$ (noise) and $\log F_{\eta L}$ (noise with a linear trend). The scale for which $\Delta = 0.05$ is the estimated crossover scale $n_\times$. For any given correlation exponent α of the noise, the crossover scale $n_\times$ exhibit a long-range power-law behavior $n_\times \sim (A_L)^\theta$, where the crossover exponent θ is a function of α [see Eq.(1.9) and Table 1.1].

with the observed values of θ obtained from our simulations [see Fig.1.4 and Table 1.1].

Finally, since the $F_L(n)$ does not depend on N_{max} as we show in Eq.(1.7), we find that $n_\times$ does not depend on N_{max}. This is a special case for linear trends and does not always hold for higher order polynomial trends.

1.4.2   DFA-2 on noise with a linear trend

Application of the DFA-2 method to noisy signals without any polynomial trends leads to scaling results identical to the scaling obtained from the DFA-1 method, with the exception of some vertical shift to lower values for the r.m.s. fluctuation function $F_\eta(n)$ [see [6]]. However, for signals which are a superposition of correlated noise and a linear trend, in contrast to the DFA-1 results presented in Fig. 1.2, $F_{\eta L}(n)$ obtained from DFA exhibit no crossovers, and is exactly equal to the r.m.s. fluctuation function $F_\eta(n)$ obtained from

Table 1.1: The crossover exponent θ from the power-law relation between the crossover scale $n_\times$ and the slope of the linear trend A_L — $n_\times \sim (A_L)^\theta$ — for different values of the correlation exponents α of the noise.

α	θ	$-1/(2-\alpha)$
0.1	-0.54	-0.53
0.3	-0.58	-0.59
0.5	-0.65	-0.67
0.7	-0.74	-0.77
0.9	-0.89	-0.91
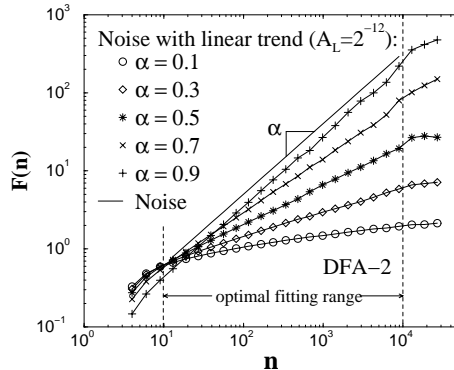
Figure 1.5: Comparison of the r.m.s. fluctuation function $F_\eta(n)$ for noise with different types of correlations (lines) and $F_{\eta L}(n)$ for the same noise with a linear trend (symbols) for DFA-2.

The slope of the linear trend is $A_L = 2^{-12}$. $F_{\eta L}(n) = F_\eta(n)$ because the integrated linear trend can be perfectly filtered out in DFA-2, thus $Y_L(i) = 0$.

DFA-2 for correlated noise without trend (see Fig. 1.5). These results indicate that a linear trend has no effect on the scaling obtained from DFA-2. The reason for this is that by design the DFA-2 method filters out linear trends, i.e. $Y_L(i) = 0$ (Eq.(1.4)) and thus $F_{\eta L}(n) = F_\eta(n)$ due to the superposition rule (Eq. (1.8)). For the same reason, polynomial

trends of order lower than ℓ superimposed on correlated noise will have no effect on scaling properties of the noise when DFA-ℓ is applied. Therefore, our results confirm that DFA method is a reliable tool to accurately quantify correlations in noisy signals embed in polynomial trends. Moreover, the reported scaling and crossover features of $F(n)$ can used to determine the order of polynomial trends present in the data.

1.5 Sinusoidal trend

In this section, we study the effect of sinusoidal trends on the scaling properties of no signals. For a signal which is a superposition of correlated noise and sinusoidal trend, find that based on the superposition rule (see 1.7.1) the DFA r.m.s. fluctuation funct can be expressed as

$$[F_{\eta S}(n)]^2 = [F_\eta(n)]^2 + [F_S(n)]^2,$$

where $F_{\eta S}(n)$ is the r.m.s. fluctuation function of noise with a sinusoidal trend, and F_S is for the sinusoidal trend. First we consider the application of DFA-1 to a sinusoi trend. Next we study the scaling behavior and the features of crossovers in $F_{\eta S}(n)$ the superposition of correlated noise and sinusoidal trend employing the superposition [Eq.(1.10)]. At the end of this section, we discuss the results obtained from higher or DFA.

1.5.1 DFA-1 on sinusoidal trend

Given a sinusoidal trend $u(i) = A_S \sin(2\pi i/T)$ $(i = 1, ..., N_{max})$, where A_S is the amplit of the signal and T is the period, we find that the r.m.s. fluctuation function $F_S(n)$ does depend on the length of the signal N_{max}, and has the same shape for different amplitu and different periods [Fig. 1.6]. We find a crossover at scale corresponding to the perio the sinusoidal trend

$$n_{2\times} \approx T,$$

and does not depend on the amplitude A_S. We call this crossover $n_{2\times}$ for convenience, as we will see later. For $n < n_{2\times}$, the r.m.s. fluctuation $F_S(n)$ exhibits an apparent scaling with the same exponent as $F_L(n)$ for the linear trend [see Eq. (1.7)]:

$$F_S(n) = k_1 \frac{A_S}{T} n^{\alpha_S} \tag{1.12}$$

where k_1 is a constant independent of the length N_{max}, of the period T and the amplitude A_S of the sinusoidal signal, and of the box size n. As for the linear trend [Eq.(1.7)], we obtain $\alpha_S = 2$ because at small scales (box size n) the sinusoidal function is dominated by a linear term. For $n > n_{2\times}$, due to the periodic property of the sinusoidal trend, $F_S(n)$ is a constant independent of the scale n:

$$F_S(n) = \frac{1}{2\sqrt{2}\pi} A_S \cdot T. \tag{1.13}$$

The period T and the amplitude A_S also affects the vertical shift of $F_S(n)$ in both regions. We note that in Eqs.(1.12) and (1.13), $F_S(n)$ is proportional to the amplitude A_S, a behavior which is also observed for the linear trend [Eq. (1.7)].

1.5.2 DFA-1 on noise with sinusoidal trend

In this section, we study how the sinusoidal trend affects the scaling behavior of noise with different type of correlations. We apply the DFA-1 method to a signal which is a superposition of correlated noise with a sinusoidal trend. We observe that there are typically three crossovers in the r.m.s. fluctuation $F_{\eta S}(n)$ at characteristic scales denoted by $n_{1\times}$, $n_{2\times}$ and $n_{3\times}$ [Fig. 1.7]. These three crossovers divide $F_{\eta S}(n)$ into four regions, as shown in Fig. 1.7(a) (the third crossover cannot be seen in Fig. 1.7(b) because its scale $n_{3\times}$ is greater than the length of the signal). We find that the first and third crossovers at scales $n_{1\times}$ and $n_{3\times}$ respectively [see Fig. 1.7] result from the competition between the effects on $F_{\eta S}(n)$ of the sinusoidal signal and the correlated noise. For $n < n_{1\times}$ (region I) and $n > n_{3\times}$ (region IV), we find that the noise has the dominating effect ($F_\eta(n) > F_S(n)$), so the behavior of $F_{\eta S}(n)$ is very close to the behavior of $F_\eta(n)$ [Eq. (1.10)]. For $n_{1\times} < n < n_{2\times}$ (region II)
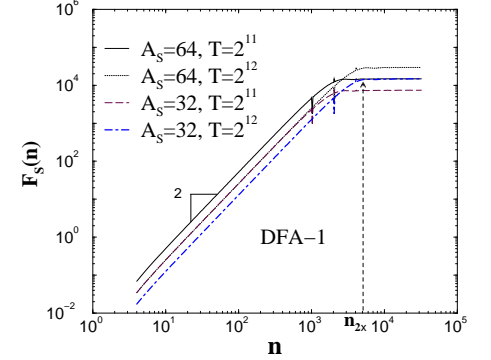
Figure 1.6: R.m.s. fluctuation function $F_S(n)$ for sinusoidal functions of length $N_{max} =$ with different amplitude A_S and period T.

All curves exhibit a crossover at $n_{2\times} \approx T/2$, with a slope $\alpha_S = 2$ for $n < n_{2\times}$, and a region for $n > n_{2\times}$. There are some spurious singularities at $n = j\frac{T}{2}$ (j is a positive integ shown by the spikes.

and $n_{2\times} < n < n_{3\times}$ (region III) the sinusoidal trend dominates ($F_S(n) > F_\eta(n)$), thus behavior of $F_{\eta S}(n)$ is close to $F_S(n)$ [see Fig. 1.7 and Fig. 1.8].

To better understand why there are different regions in the behavior of $F_{\eta S}(n)$, we c sider the detrended fluctuation function [Eq. (1.4)] of the correlated noise $Y_\eta(i)$, and of noise with sinusoidal trend $Y_{\eta S}$. In Fig. 1.8 we compare $Y_\eta(i)$ and $Y_{\eta S}(i)$ for anticorrela and correlated noise in the four different regions. For very small scales $n < n_{1\times}$, the eff of the sinusoidal trend is not pronounced, $Y_{\eta S}(i) \approx Y_\eta(i)$, indicating that in this scale reg the signal can be considered as noise fluctuating around a constant trend which is filte out by the DFA-1 procedure [Fig. 1.8(a)(b)]. Note, that the behavior of $Y_{\eta S}$ [Fig. 1.8 is identical to the behavior of $Y_{\eta L}$ [Fig. 1.3(b)], since both a sinusoidal with a large per T and a linear trend with small slope A_L can be well approximated by a constant tr for $n < n_{1\times}$. For small scales $n_{1\times} < n < n_{2\times}$ (region II), we find that there is a domin quadratic background for $Y_{\eta S}(i)$ [Fig. 1.8(d)]. This quadratic background is due to integration procedure in DFA-1, and is represented by the detrended fluctuation funct
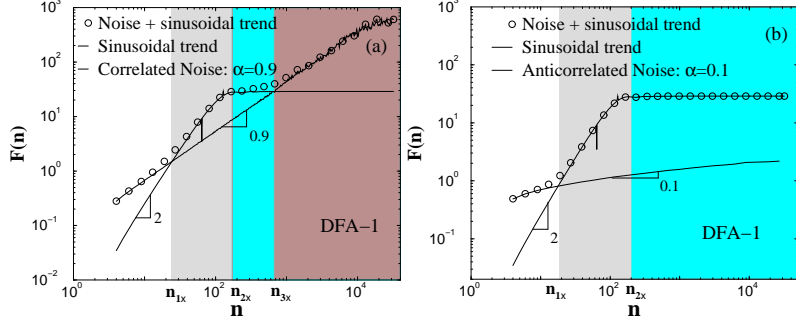
Figure 1.7: Crossover behavior of the root mean square fluctuation function $F_{\eta S}(n)$ (circles) for correlated noise (of length $N_{max} = 2^{17}$) with a superposed sinusoidal function characterized by period $T = 128$ and amplitude $A_S = 2$.

The r.m.s. fluctuation function $F_\eta(n)$ for noise (thick line) and $F_S(n)$ for the sinusoidal trend (thin line) are shown for comparison. (a) $F_{\eta S}(n)$ for correlated noise with $\alpha = 0.9$. (b) $F_{\eta S}(n)$ for anticorrelated noise with $\alpha = 0.9$. There are three crossovers in $F_{\eta S}(n)$, at scales $n_{1\times}$, $n_{2\times}$ and $n_{3\times}$ (the third crossover can not be seen in (b) because it occurs at scale larger than the length of the signal). For $n < n_{1\times}$ and $n > n_{3\times}$, the noise dominates and $F_{\eta S}(n) \approx F_\eta(n)$ while for $n_{1\times} < n < n_{3\times}$, the sinusoidal trend dominates and $F_{\eta S}(n) \approx F_S(n)$. The crossovers at $n_{1\times}$ and $n_{3\times}$ are due to the competition between the correlated noise and the sinusoidal trend [see Fig. 1.8], while the crossover at $n_{2\times}$ relates only to the period T of the sinusoidal [Eq. (1.11)].

of the sinusoidal trend $Y_S(i)$. It is similar to the quadratic background observed for linear trend $Y_{\eta L}(i)$ [Fig. 1.3(d)] — i.e. for $n_{1\times} < n < n_{2\times}$ the sinusoidal trend behaves as a linear trend and $Y_S(i) \approx Y_L(i)$. Thus in region II the "linear trend" effect of the sinusoidal is dominant, $Y_S > Y_\eta$, which leads to $F_{\eta S}(n) \approx F_S(n)$. This explains also why $F_{\eta S}(n)$ for $n < n_{2\times}$ (Fig. 1.7) exhibits crossover behavior similar to the one of $F_{\eta L}(n)$ observed for noise with a linear trend. For $n_{2\times} < n < n_{3\times}$ (region III) the sinusoidal behavior is strongly pronounced [Fig. 1.8(f)], $Y_S(i) \gg Y_\eta(i)$, and $Y_{\eta S}(i) \approx Y_S(i)$ changes periodically with period equal to the period of the sinusoidal trend T. Since $Y_{\eta S}(i)$ is bounded between a minimum
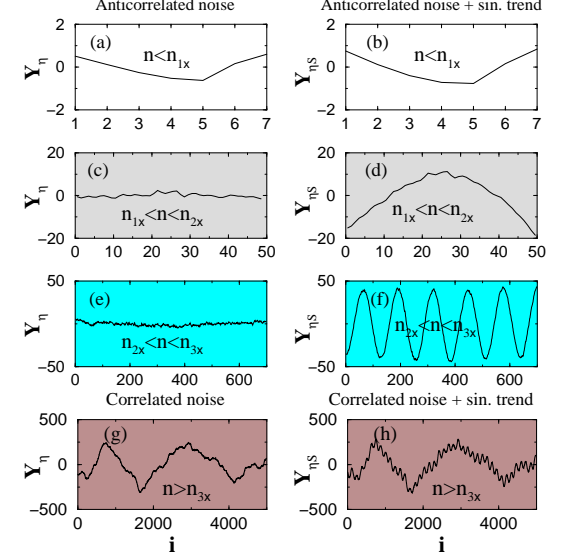
Figure 1.8: Comparison of the detrended fluctuation function for noise, $Y_\eta(i)$ and noise with sinusoidal trend, $Y_{\eta S}(i)$ in four regions.

The same signals as in Fig. 1.7 are used. Panels (a)-(f) correspond to Fig. 1.7(b) for anticorrelated noise with exponent $\alpha = 0.1$, and panels (g)-(h) correspond to the Fig. 1.7 for correlated noise with exponent $\alpha = 0.9$. (a)-(b) For all scales $n < n_{1\times}$, (c)(d) $n_{2\times} > n > n_{1\times}$, (e)(f) For $n_{2\times} < n < n_{3\times}$ (i.e. $n \gg T/2$), (g)(h) for $n > n_{3\times}$.

and a maximum value, $F_{\eta S}(n)$ cannot increase and exhibits a flat region (Fig. 1.7). At very large scales, $n > n_{3\times}$, the noise effect is again dominant ($Y_S(i)$ remains bounded, while grows when increasing the scale) which leads to $F_{\eta S}(n) \approx F_\eta(n)$, and a scaling behavior corresponding to the scaling of the correlated noise.

First, we consider $n_{1\times}$. Surprisingly, we find that for noise with any given correlation exponent α the crossover scale $n_{1\times}$ exhibits long-range power-law dependence of the period T — $n_{1\times} \sim T^{\theta_{T1}}$, and the amplitude A_S — $n_{1\times} \sim (A_S)^{\theta_{A1}}$ of the sinusoidal trend [Fig. 1.9(a) and (b)]. We find that the "crossover exponents" θ_{T1} and θ_{A1} have the same
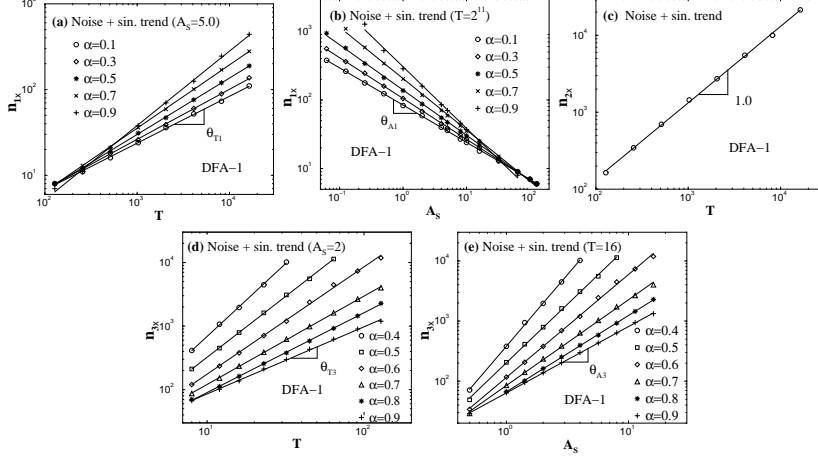
Figure 1.9: Dependence of the three crossovers in $F_{\eta S}(n)$ for noise with a sinusoidal trend on the period T, and amplitude A_S of the sinusoidal trend.

(a) Power-law relation between the first crossover scale $n_{1\times}$ and the period T for fixed amplitude A_S and varying correlation exponent α, (b) Power-law relation between the first crossover $n_{1\times}$ and the amplitude of the sinusoidal trend A_S for fixed period T and varying correlation exponent α, (c) The second crossover scale $n_{2\times}$, (d) Power-law relation between the third crossover $n_{3\times}$ and T for fixed amplitude A_S and varying α trend, (e) Power-law relation between the third crossover $n_{3\times}$ and A_S for fixed T and varying α.

magnitude but different sign — θ_{T1} is positive while θ_{A1} is negative. We also find that the magnitude of θ_{T1} and θ_{A1} increases for the larger values of the correlation exponents α of the noise. We present the values of θ_{T1} and θ_{A1} for different correlation exponent α in Table 1.2. To understand these power-law relations between $n_{1\times}$ and T, and between $n_{1\times}$ and A_S, and also how the crossover scale $n_{1\times}$ depends on the correlation exponent α we employ the superposition rule [Eq. 1.10] and estimate $n_{1\times}$ analytically as the first intercept $n_{1\times}^{th}$ of $F_\eta(n)$ and $F_S(n)$. From Eqs. (1.12) and (1.6), we obtain the following dependence of $n_{1\times}$ on T, A_S and α:

$$n_{1\times} = \left(\frac{b_0}{k_1}\frac{T}{A_S}\right)^{1/(2-\alpha)} \tag{1.14}$$

From this analytical calculation we obtain the following relation between the two crosso exponents θ_{T1} and θ_{A1} and the correlation exponent α: $\theta_{T1} = -\theta_{A1} = 1/(2-\alpha)$, wh is in a good agreement with the observed values of θ_{T1}, θ_{A1} obtained from simulations Fig. 1.9(a) (b) and Table 1.2].

Next, we consider $n_{2\times}$. Our analysis of the r.m.s. fluctuation function $F_S(n)$ for sinusoidal signal in Fig. 1.6 suggests that the crossover scale $F_S(n)$ does not depend on amplitude A_S of the sinusoidal. The behavior of the r.m.s. fluctuation function $F_{\eta S}(n)$ noise with superimposed sinusoidal trend in Fig. 1.7(a) and (b) indicates that $n_{2\times}$ d not depend on the correlation exponent α of the noise, since for both correlated ($\alpha = $ and anticorrelated ($\alpha = 0$) noise (T and A_S are fixed), the crossover scale $n_{2\times}$ rem unchanged. We find that $n_{2\times}$ depends **only** on the period T of the sinusoidal trend exhibits a long-range power-law behavior $n_{2\times} \sim T^{\theta_{T2}}$ with a crossover exponent θ_{T2} (Fig. 1.9(c)) which is in agreement with the prediction of Eq.(1.11).

For the third crossover scale $n_{3\times}$, as for $n_{1\times}$ we find a power-law dependence on the riod T, $n_{3\times} \sim T^{\theta_{T3}}$, and amplitude A_S, $n_{3\times} \sim (A_S)^{\theta_{A3}}$, of the sinusoidal trend [see Fig. 1.9 and (e)]. However, in contrast to the $n_{1\times}$ case, we find that the crossover exponents θ and θ_{A3} are equal and positive with decreasing values for increasing correlation expone α. In Table 1.3, we present the values of these two exponents for different correlation ex nent α. To understand how the scale $n_{3\times}$ depends on T, A_S and the correlation expon α simultaneously, we again employ the superposition rule [Eq. (1.10)] and estimate $n_{3\times}$ the second intercept $n_{3\times}^{th}$ of $F_\eta(n)$ and $F_S(n)$. From Eqs. (1.13) and (1.6), we obtain following dependence:

$$n_{3\times} = \left(\frac{1}{2\sqrt{2}\pi b_0}A_S T\right)^{1/\alpha}. \tag{1.}$$

From this analytical calculation we obtain $\theta_{T3} = \theta_{A3} = 1/\alpha$ which is in good agreem with the values of θ_{T3} and θ_{A3} observed from simulations [Table 1.3].

Finally, our simulations show that all three crossover scales $n_{1\times}$, $n_{2\times}$ and $n_{3\times}$ do depend on the length of the signal N_{max}, since $F_\eta(n)$ and $F_S(n)$ do not depend on N_{max} shown in Eqs. (1.6), (1.10), (1.12), and (1.13).

Table 1.2: The crossover exponents θ_{T1} and θ_{A1} characterizing the power-law dependence of $n_{1\times}$ on the period T and amplitude A_{S} obtained from simulations: $n_{1\times} \sim T^{\theta_{\text{T1}}}$ and $n_{1\times} \sim (A_{\text{S}})^{\theta_{\text{A1}}}$ for different value of the correlation exponent α of noise.

α	θ_{T1}	$-\theta_{\text{A1}}$	$1/(2-\alpha)$
0.1	0.55	0.54	0.53
0.3	0.58	0.59	0.59
0.5	0.66	0.66	0.67
0.7	0.74	0.75	0.77
0.9	0.87	0.90	0.91

Table 1.3: The crossover exponents θ_{T3} and θ_{A3} for the power-law relations: $n_{3\times} \sim T^{\theta_{\text{T3}}}$ and $n_{3\times} \sim (A_{\text{S}})^{\theta_{\text{A3}}}$ for different value of the correlation exponent α of noise.

α	θ_{T3}	θ_{A3}	$1/\alpha$
0.4	2.29	2.38	2.50
0.5	1.92	1.95	2.00
0.6	1.69	1.71	1.67
0.7	1.39	1.43	1.43
0.8	1.26	1.27	1.25
0.9	1.06	1.10	1.11

1.5.3 Higher order DFA on pure sinusoidal trend

In the previous Sec. 1.5.2, we discussed how sinusoidal trends affect the scaling behavior of correlated noise when the DFA-1 method is applied. Since DFA-1 removes only constant trends in data, it is natural to ask how the observed scaling results will change when we apply DFA of order ℓ designed to remove polynomial trends of order lower than ℓ. In this section, we first consider the r.m.s. fluctuation F_{S} for a sinusoidal signal and then we study the scaling and crossover properties of $F_{\eta\text{S}}$ for correlated noise with superimposed sinusoidal signal when higher order DFA is used.

We find that the r.m.s. fluctuation function F_{S} does not depend on the length of the signal N_{max}, and preserves a similar shape when different order-ℓ DFA method is used
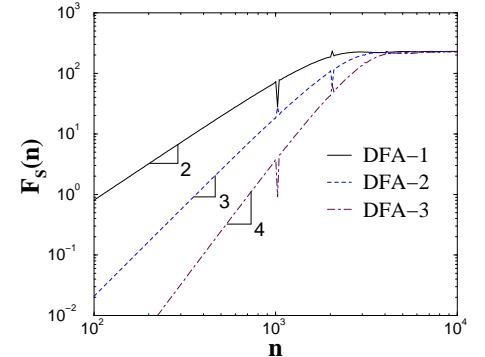
Figure 1.10: Comparison of the results of different order DFA on a sinusoidal trend. The sinusoidal trend is given by the function $64\sin(2\pi i/2^{11})$ and the length of the signal $N_{max} = 2^{17}$. The spurious singularities (spikes) arise from the discrete data we use for sinusoidal function.

[Fig. 1.10]. In particular, F_{S} exhibits a crossover at a scale $n_{2\times}$ proportional to the period T of the sinusoidal: $n_{2\times} \sim T^{\theta_{\text{T2}}}$ with $\theta_{\text{T2}} \approx 1$. The crossover scale shifts to larger value for higher order ℓ [Fig. 1.6 and Fig. 1.10]. For the scale $n < n_{2\times}$, F_{S} exhibits an apparent scaling: $F_{\text{S}} \sim n^{\alpha_{\text{S}}}$ with an effective exponent $\alpha_{\text{S}} = \ell + 1$. For DFA-1, we have $\ell = 1$ and recover $\alpha_{\text{S}} = 2$ as shown in Eq. (1.12). For $n > n_{2\times}$, $F_{\text{S}}(n)$ is a constant independent of the scale n, and of the order ℓ of the DFA method in agreement with Eq. (1.13).

Next, we consider $F_{\eta\text{S}}(n)$ when DFA-ℓ with a higher order ℓ is used. We find that for all orders ℓ, $F_{\eta\text{S}}(n)$ does not depend on the length of the signal N_{max} and exhibits three crossovers — at small, intermediate and large scales — similar behavior is reported for DFA-1 in Fig. 1.7. Since the crossover at small scales, $n_{1\times}$, and the crossover at large scale $n_{3\times}$, result from the "competition" between the scaling of the correlated noise and the effect of the sinusoidal trend (Figs. 1.7 and 1.8), using the superposition rule [Eq. (1.10)] we can estimate $n_{1\times}$ and $n_{3\times}$ as the intercepts of $F_{\eta}(n)$ and $F_{\text{S}}(n)$ for the general case of DFA-ℓ.

For $n_{1\times}$ we find the following dependence on the period T, amplitude A_{S}, the correlation

exponent α of the noise, and the order ℓ of the DFA-ℓ method:

$$n_{1\times} \sim (T/A_{\text{S}})^{1/(\ell+1-\alpha)} \tag{1.16}$$

For DFA-1, we have $\ell = 1$ and we recover Eq. (1.14). In addition, $n_{1\times}$ is shifted to larger scales when higher order DFA-ℓ is applied, due to the fact that the value of $F_{\text{S}}(n)$ decreases when ℓ increases ($\alpha_{\text{S}} = \ell + 1$, see Fig. 1.10).

For the third crossover observed in $F_{\eta \text{S}}(n)$ at large scale $n_{3\times}$ we find for all orders ℓ of the DFA-ℓ the following scaling relation:

$$n_{3\times} \sim (TA_{\text{S}})^{1/\alpha}. \tag{1.17}$$

Since the scaling function $F_\eta(n)$ for correlated noise shifts vertically to lower values when higher order DFA-ℓ is used, $n_{3\times}$ exhibits a slight shift to larger scales.

For the crossover $n_{2\times}$ in $F_{\eta \text{S}}(n)$ at $F_{\eta \text{S}}(n)$ at intermediate scales, we find: $n_{2\times} \sim T$. This relation is independent of the order ℓ of the DFA and is identical to the relation found for $F_{\text{S}}(n)$ [Eq. (1.11)]. $n_{2\times}$ also exhibits a shift to larger scales when higher order DFA is used [see Fig. 1.10].

The reported here features of the crossovers in $F_{\eta \text{S}}(n)$ can be used to identify low-frequency sinusoidal trends in noisy data, and to recognize their effects on the scaling properties of the data. This information may be useful when quantifying correlation properties in data by means of scaling analysis.

1.6 Power-law trend

In this section we study the effect of power-law trends on the scaling properties of noisy signals. We consider the case of correlated noise with superposed power-law trend $u(i) = A_{\text{P}} i^\lambda$, when A_{P} is a positive constant, $i = 1, ..., N_{max}$, and N_{max} is the length of the signal. We find that when the DFA-1 method is used, the r.m.s. fluctuation function $F_{\eta \text{P}}(n)$ exhibits a crossover between two scaling regions [Fig. 1.11]. This behavior results from the fact that at different scales n, either the correlated noise or the power-law trend is dominant, and
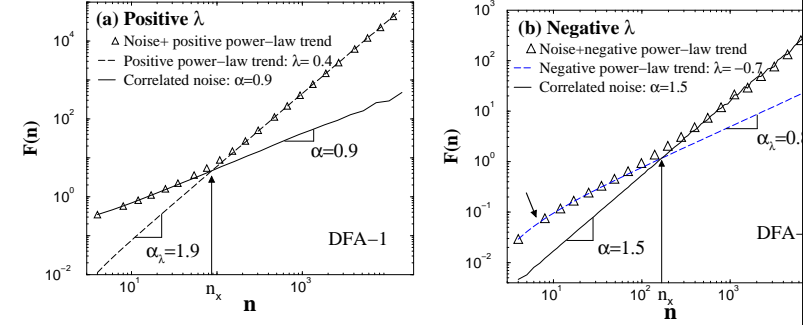
Figure 1.11: Crossover behavior of the r.m.s. fluctuation function $F_{\eta \text{P}}(n)$ (circles) correlated noise (of length $N_{max} = 2^{17}$) with a superimposed power-law trend $u(i) = A_{\text{P}}$ The r.m.s. fluctuation function $F_\eta(n)$ for noise (solid line) and the r.m.s. fluctuation fu tion $F_{\text{P}}(n)$ (dash line) are also shown for comparison. (a) $F_{\eta \text{P}}(n)$ for noise with correlat exponent $\alpha_\lambda = 0.9$, and power-law trend with amplitude $A_{\text{P}} = 1000/(N_{max})^{0.4}$ and p tive power $\lambda = 0.4$; (b) $F_{\eta \text{P}}(n)$ for Brownian noise (integrated white noise, $\alpha_\lambda = 1.5$), power-law trend with amplitude $A_{\text{P}} = 0.01/(N_{max})^{-0.7}$ and negative power $\lambda = -0.7$.

can be predicted by employing the superposition rule:

$$[F_{\eta \text{P}}(n)]^2 = [F_\eta(n)]^2 + [F_{\text{P}}(n)]^2, \tag{1.}$$

where $F_\eta(n)$ and $F_{\text{P}}(n)$ are the r.m.s. fluctuation function of noise and the power-trend respectively, and $F_{\eta \text{P}}(n)$ is the r.m.s. fluctuation function for the superpositio the noise and the power-law trend. Since the behavior of $F_\eta(n)$ is known (Eq. (1.6) Sec. 1.7.1), we can understand the features of $F_{\eta \text{P}}(n)$, if we know how $F_{\text{P}}(n)$ depends on characteristics of the power-law trend. We note that the scaling behavior of $F_{\eta \text{P}}(n)$ displa in Fig. 1.11(a) is to some extent similar to the behavior of the r.m.s. fluctuation funct $F_{\eta \text{L}}(n)$ for correlated noise with a linear trend [Fig. 1.2] — e.g. the noise is dominant small scales n, while the trend is dominant at large scales. However, the behavior $F_{\text{P}}(n)$ more complex than that of $F_{\text{L}}(n)$ for the linear trend, since the effective exponent α_λ $F_{\text{P}}(n)$ can depend on the power λ of the power-law trend. In particular, for negative val

of λ, $F_\mathrm{P}(n)$ can become dominated at small scales (Fig. 1.11(b)) while $F_\eta(n)$ dominates at large scales — a situation completely opposite of noise with linear trend (Fig. 1.2) or with power-law trend with positive values for the power λ. Moreover, $F_\mathrm{P}(n)$ can exhibit crossover behavior at small scales [Fig. 1.11(b)] for negative λ which is not observed for positive λ. In addition $F_\mathrm{P}(n)$ depends on the order ℓ of the DFA method and the length N_{max} of the signal. We discuss the scaling features of the power-law trends in the following three subsections.

1.6.1 Dependence of $F_\mathrm{P}(n)$ on the power λ

First we study how the r.m.s. fluctuation function $F_\mathrm{P}(n)$ for a power-law trend $u(i) = A_\mathrm{P} i^\lambda$ depends on the power λ. We find that

$$F_\mathrm{P}(n) \sim A_\mathrm{P} n^{\alpha_\lambda}, \tag{1.19}$$

where α_λ is the effective exponent for the power-law trend. For positive λ we observe no crossovers in $F_\mathrm{P}(n)$ (Fig. 1.11(a)). However, for negative λ there is a crossover in $F_\mathrm{P}(n)$ at small scales n (Fig. 1.11(b)), and we find that this crossover becomes even more pronounced with decreasing λ or increasing the order ℓ of the DFA method, and is also shifted to larger scales [Fig. 1.12(a)].

Next, we study how the effective exponent α_λ for $F_\mathrm{P}(n)$ depends on the value of the power λ for the power-law trend. We examine the scaling of $F_\mathrm{P}(n)$ and estimate α_λ for $-4 < \lambda < 4$. In the cases when $F_\mathrm{P}(n)$ exhibits a crossover, in order to obtain α_λ we fit the range of larger scales to the right of the crossover. We find that for any order ℓ of the DFA-ℓ method there are three regions with different relations between α_λ and λ [Fig. 1.12(b)]:

(i) $\alpha_\lambda \approx \ell + 1$ for $\lambda > \ell - 0.5$ (region I);

(ii) $\alpha_\lambda \approx \lambda + 1.5$ for $-1.5 \leq \lambda \leq \ell - 0.5$ (region II);

(iii) $\alpha_\lambda \approx 0$ for $\lambda < -1.5$ (region III).
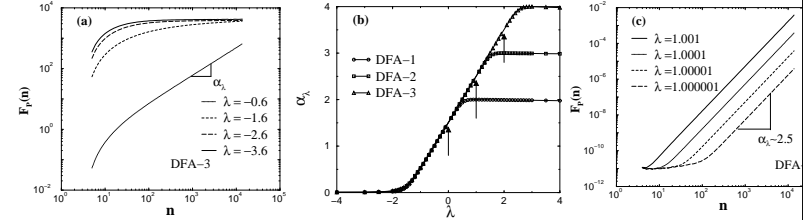
Figure 1.12: Scaling behavior of r.m.s. fluctuation function $F_\mathrm{P}(n)$ for power-law trend $u(i) \sim i^\lambda$, where $i = 1, ..., N_{max}$ and $N_{max} = 2^{17}$ is the length of the signal.
(a) For $\lambda < 0$, $F_\mathrm{P}(n)$ exhibits crossover at small scales which is more pronounced with increasing the order ℓ of DFA-ℓ and decreasing the value of λ. (b) Dependence of effective exponent α_λ on the power λ for different order $\ell = 1, 2, 3$ of the DFA method. (c) Asymptotic behavior near integer values of λ. $F_\mathrm{P}(n)$ is plotted for $\lambda \to 1$ when DFA-2 is used.

Note, that for integer values of the power λ ($\lambda = 0, 1, ..., m - 1$), i.e. polynomial trends of order $m - 1$, the DFA-ℓ method of order $\ell > m - 1$ (ℓ is also an integer) leads to $F_\mathrm{P}(n) \approx 0$ since DFA-ℓ is designed to remove polynomial trends. Thus for a integer values of the power λ there is no scaling and the effective exponent α_λ is not defined if a DFA-ℓ method of order $\ell > \lambda$ is used [Fig. 1.12]. However, it is of interest to examine the asymptotic behavior of the scaling of $F_\mathrm{P}(n)$ when the value of the power λ is close to an integer. In particular , we consider how the scaling of $F_\mathrm{P}(n)$ obtained from DFA-2 method changes when $\lambda \to 1$ [Fig. 1.12(c)]. Surprisingly, we find that even though the values of $F_\mathrm{P}(n)$ are very small at large scales, there is a scaling for $F_\mathrm{P}(n)$ with a smooth convergence to the effective exponent $\alpha_\lambda \to 2.5$ when $\lambda \to 1$, according to the dependence $\alpha_\lambda \approx \lambda + 1.5$ established for region II [Fig. 1.12(b)]. At smaller scales there is a flat region which is due to the fact that the fluctuation function $Y(i)$ (Eq. (1.4)) is smaller than the precision of the numerical simulation.

1.6.2 Dependence of $F_P(n)$ on the order ℓ of DFA

Another factor that affects the r.m.s. fluctuation function of the power-law trend $F_P(n)$, is the order ℓ of the DFA method used. We first take into account that:

(1) for integer values of the power λ, the power-law trend $u(i) = A_P i^\lambda$ is a polynomial trend which can be perfectly filtered out by the DFA method of order $\ell > \lambda$, and as discussed in Sec. 1.4.2 and Sec. 1.6.1 [see Fig. 1.12(b) and (c)], there is no scaling for $F_P(n)$. Therefore, in this section we consider only non-integer values of λ.

(2) for a given value of the power λ, the effective exponent α_λ can take different values depending on the order ℓ of the DFA method we use [see Fig. 1.12] — e.g. for fixed $\lambda > \ell - 0.5$, $\alpha_\lambda \approx \ell + 1$. Therefore, in this section, we consider only the case when $\lambda < \ell - 0.5$ (Region II and III).

Since higher order DFA-ℓ provides a better fit for the data, the fluctuation function $Y(i)$ (Eq. (1.4)) decreases with increasing order ℓ. This leads to a vertical shift to smaller values of the r.m.s. fluctuation function $F(n)$ (Eq. (1.3)). Such a vertical shift is observed for the r.m.s. fluctuation function $F_\eta(n)$ for correlated noise (see [62]), as well as for the r.m.s. fluctuation function of power-law trend $F_P(n)$. Here we ask how this vertical shift in $F_\eta(n)$ and $F_P(n)$ depends on the order ℓ of the DFA method, and if this shift has different properties for $F_\eta(n)$ compared to $F_P(n)$. This information can help identify power-law trends in noisy data, and can be used to differentiate crossovers separating scaling regions with different types of correlations, and crossovers which are due to effects of power-law trends.

We consider correlated noise with a superposed power-law trend, where the crossover in $F_{\eta P}(n)$ at large scales n results from the dominant effect of the power-law trend — $F_{\eta P}(n) \approx F_P(n)$ (Eq. (1.18) and Fig. 1.11(a)). We choose the power $\lambda < 0.5$, a range where for all orders ℓ of the DFA method the effective exponent α_λ of $F_P(n)$ remains the same — i.e. $\alpha_\lambda = \lambda + 1.5$ (region II in Fig. 1.12(b)). For a superposition of an anticorrelated noise and power-law trend with $\lambda = 0.4$, we observe a crossover in the scaling behavior of
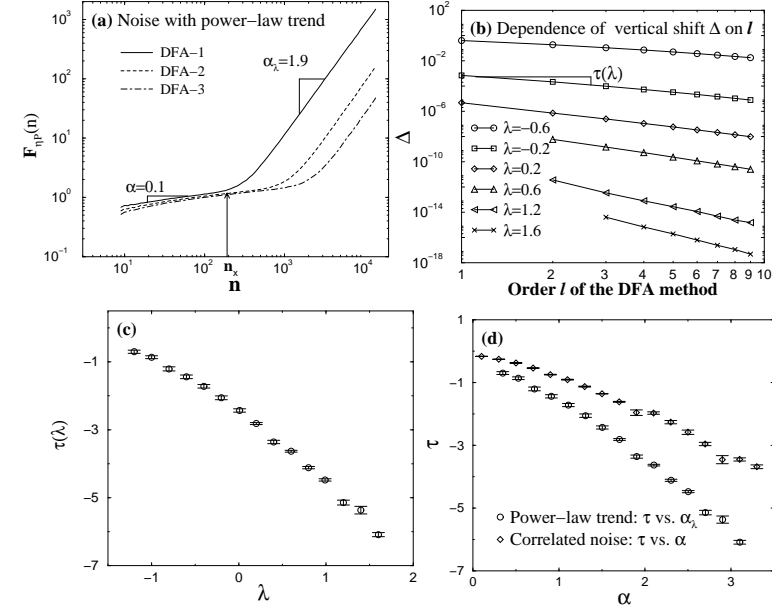
Figure 1.13: Effect of higher order DFA-ℓ on the r.m.s. fluctuation function $F_{\eta P}(n)$ correlated noise with superimposed power-law trend.

(a) $F_{\eta P}(n)$ for anticorrelated noise with correlation exponent $\alpha = 0.1$ and a power-$u(i) = A_P i^\lambda$, where $A_P = 25/(N_{max})^{0.4}$, $N_{max} = 2^{17}$ and $\lambda = 0.4$. Results for differ order $\ell = 1, 2, 3$ of the DFA method show (i) a clear crossover from a region at small sc where the noise dominates $F_{\eta P}(n) \approx F_\eta(n)$, to a region at larger scales where the power-trend dominates $F_{\eta P}(n) \approx F_P(n)$, and (ii) a vertical shift Δ in $F_{\eta P}$ with increasing ℓ. Dependence of the vertical shift Δ in the r.m.s. fluctuation function $F_P(n)$ for power-trend on the order ℓ of DFA-ℓ for different values of λ: $\Delta \sim \ell^{\tau(\lambda)}$. We define the vert shift Δ as the y-intercept of $F_P(n)$: $\Delta \equiv F_P(n = 1)$. (c) Dependence of τ on the powe (error bars indicate the regression error for the fits of $\Delta(l)$ in (b)). (d) Comparison of $\tau($ for $F_P(n)$ and $\tau(\alpha)$ for $F_\eta(n)$.

$F_{\eta P}(n)$, from a scaling region characterized by the correlation exponent $\alpha = 0.1$ of the no where $F_{\eta P}(n) \approx F_\eta(n)$, to a region characterized by an effective exponent $\alpha_\lambda = 1.9$, wl

$F_{\eta P}(n) \approx F_P(n)$, for all orders $\ell = 1, 2, 3$ of the DFA-ℓ method [Fig. 1.13(a)]. We also find that the crossover of $F_{\eta P}(n)$ shifts to larger scales when the order ℓ of DFA-ℓ increases, and that there is a vertical shift of $F_{\eta P}(n)$ to lower values. This vertical shift in $F_{\eta P}(n)$ at large scales, where $F_{\eta P}(n) = F_P(n)$, appears to be different in magnitude when different order ℓ of the DFA-ℓ method is used [Fig. 1.13(a)]. We also observe a less pronounced vertical shift at small scales where $F_{\eta P}(n) \approx F_{\eta}(n)$.

Next, we ask how these vertical shifts depend on the order ℓ of DFA-ℓ. We define the vertical shift Δ as the y-intercept of $F_P(n)$: $\Delta \equiv F_P(n = 1)$. We find that the vertical shift Δ in $F_P(n)$ for power-law trend follows a power law: $\Delta \sim \ell^{\tau(\lambda)}$. We tested this relation for orders up to $\ell = 10$, and we find that it holds for different values of the power λ of the power-law trend [Fig. 1.13(b)]. Using Eq. (1.19) we can write: $F_P(n)/F_P(n = 1) = n^{\alpha\lambda}$, i.e. $F_P(n) \sim F_P(n = 1)$. Since $F_P(n = 1) \equiv \Delta \sim \ell^{\tau(\lambda)}$ [Fig. 1.13(b)], we find that:

$$F_P(n) \sim \ell^{\tau(\lambda)}. \tag{1.20}$$

We also find that the exponent τ is negative and is a decreasing function of the power λ [Fig. 1.13(c)]. Because the effective exponent α_λ which characterizes $F_P(n)$ depends on the power λ [see Fig. 1.12(b)], we can express the exponent τ as a function of α_λ as we show in Fig. 1.13(d). This representation can help us compare the behavior of the vertical shift Δ in $F_P(n)$ with the shift in $F_{\eta}(n)$. For correlated noise with different correlation exponent α, we observe a similar power-law relation between the vertical shift in $F_{\eta}(n)$ and the order ℓ of DFA-ℓ: $\Delta \sim \ell^{\tau(\alpha)}$, where τ is also a negative exponent which decreases with α. In Fig. 1.13(d) we compare $\tau(\alpha_\lambda)$ for $F_P(n)$ with $\tau(\alpha)$ for $F_{\eta}(n)$, and find that for any $\alpha_\lambda = \alpha$, $\tau(\alpha_\lambda) < \tau(\alpha)$. This difference between the vertical shift for correlated noise and for a power-law trend can be utilized to recognize effects of power-law trends on the scaling properties of data.

1.6.3 Dependence of $F_P(n)$ on the signal length N_{max}

Here, we study how the r.m.s. fluctuation function $F_P(n)$ depends on the length N_{max} of the power-law signal $u(i) = A_P i^\lambda$ $(i = 1, ..., N_{max})$. We find that there is a vertical shift

in $F_P(n)$ with increasing N_{max} [Fig. 1.14(a)]. We observe that when doubling the len N_{max} of the signal the vertical shift in $F_P(n)$, which we define as $F_P^{2N_{max}}/F_P^{N_{max}}$, rema the same, independent of the value of N_{max}. This suggests a power-law dependence $F_P(n)$ on the length of the signal:

$$F_P(n) \sim (N_{max})^\gamma, \tag{1.}$$

where γ is an effective scaling exponent.

Next, we ask if the vertical shift depends on the power λ of the power-law trend. W doubling the length N_{max} of the signal, we find that for $\lambda < \ell - 0.5$, where ℓ is the orde the DFA method, the vertical shift is a constant independent of λ [Fig. 1.14(b)]. Since value of the vertical shift when doubling the length N_{max} is 2^γ (from Eq. (1.21)), the res in Fig. 1.14(b) show that γ is independent of λ when $\lambda < \ell - 0.5$, and that $-\log 2^\gamma \approx -0$ i.e. the effective exponent $\gamma \approx -0.5$.

For $\lambda > \ell - 0.5$, when doubling the length N_{max} of the signal, we find that the vert shift 2^γ exhibits the following dependence on λ: $-\log_{10} 2^\gamma = \log_{10} 2^{\lambda-\ell}$, and thus effective exponent γ depends on λ — $\gamma = \lambda - \ell$. For positive integer values of λ $(\lambda = \ell)$, find that $\gamma = 0$, and there is no shift in $F_P(n)$, suggesting that $F_P(n)$ does not depend the length N_{max} of the signal, when DFA of order ℓ is used [Fig. 1.14]. Finally, we note t depending on the effective exponent γ, i.e. on the order ℓ of the DFA method and the va of the power λ, the vertical shift in the r.m.s. fluctuation function $F_P(n)$ for power-trend can be positive $(\lambda > \ell)$, negative $(\lambda < \ell)$, or zero $(\lambda = \ell)$.

1.6.4 Combined effect on $F_P(n)$ of λ, ℓ and N_{max}

We have seen that, taking into account the effects of the power λ (Eq. (1.19)), the ord of DFA-ℓ (Eq. (1.20)) and the effect of the length of the signal N_{max} (Eq. (1.21)), we re the following expression for the r.m.s. fluctuation function $F_P(n)$ for a power-law tr $u(i) = A_P i^\lambda$:
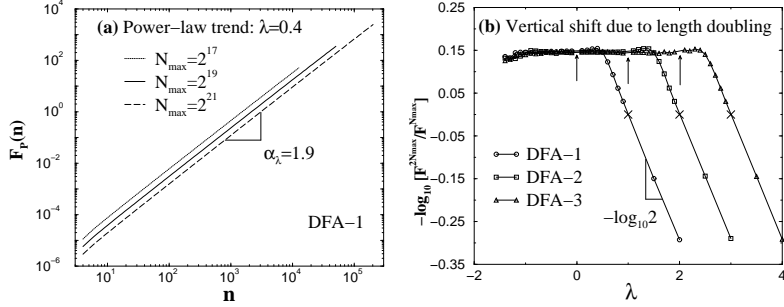
Figure 1.14: Dependence of the r.m.s. fluctuation function $F_{\mathrm{P}}(n)$ for power-law trend $u(i) = A_{\mathrm{P}}i^\lambda$, where $i = 1, ..., N_{max}$, on the length of the trend N_{max}.

(a) A vertical shift is observed in $F_{\mathrm{P}}(n)$ for different values of N_{max} — N_{1max} and N_{2max}. The figure shows that the vertical shift, defined as $F_{\mathrm{P}}^{N_{1max}}(n)/F_{\mathrm{P}}^{N_{2max}}(n)$, does not depend on N_{max} but only on the ratio N_{1max}/N_{2max}, suggesting that $F_{\mathrm{P}}(n) \sim (N_{max})^\gamma$. (b) Dependence of the vertical shift on the power λ.

$$F_{\mathrm{P}}(n) \sim A_{\mathrm{P}} \cdot n^{\alpha_\lambda} \cdot \ell^{\tau(\lambda)} \cdot (N_{max})^{\gamma(\lambda)}, \tag{1.22}$$

For correlated noise, the r.m.s. fluctuation function $F_\eta(n)$ depends on the box size n (Eq. (1.6)) and on the order ℓ of DFA-ℓ (Sec. 1.6.2 and Fig. 1.13(a), (d)), and does not depend on the length of the signal N_{max}. Thus we have the following expression for $F_\eta(n)$

$$F_\eta(n) \sim n^\alpha \ell^{\tau(\alpha)}, \tag{1.23}$$

To estimate the crossover scale $n_\times$ observed in the apparent scaling of $F_{\eta\mathrm{P}}(n)$ for a correlated noise superposed with a power-law trend [Fig. 1.11(a), (b) and Fig. 1.13(a)], we employ the superposition rule (Eq. (1.18)). From Eq. (1.22) and Eq. (1.23), we obtain $n_\times$ as the intercept between $F_{\mathrm{P}}(n)$ and $F_\eta(n)$:

$$n_\times \sim \left[A l^{\tau(\lambda)-\tau(\alpha)} (N_{max})^\gamma \right]^{1/(\alpha-\alpha_\lambda)}. \tag{1.24}$$

To test the validity of this result, we consider the case of correlated noise with a linear trend. For the case of a linear trend ($\lambda = 1$) when DFA-1 ($\ell = 1$) is applied, we have $\alpha_\lambda = 2$

(see Sec. 1.6.1, Fig. 1.12(b)). Since in this case $\lambda = \ell = 1 > \ell - 0.5$ we have $\gamma = \lambda - \ell$ (see Sec.1.6.3 Fig. 1.14(b)), and from Eq. (1.24) we recover Eq. (1.9).

1.7 General rules

1.7.1 Superposition rule

Here we show how the DFA results for any two signals f and g [denoted as $F_f(n)$ and F_g relate with the DFA result for the sum of these two signals $f+g$ [denoted as $F_{f+g}(n)$, wher is the box length (scale of analysis)]. In the general cases, we find $|F_f - F_g| \le F_{f+g} \le F_f +$ When the two signals are not correlated, we find that the following *superposition rul* valid: $F_{f+g}^2 = F_f^2 + F_g^2$. Here we derive these relations.

First we summarize again the procedure of the DFA method [1]. It includes the lowing steps: starting with an original signal $u(i)$ of length N_{max}, we integrate and obt $y(k) = \sum_{j=1}^{k} (u(j) - \langle u \rangle)$, where $\langle u \rangle$ is the mean of $u(i)$. Next, we divide $y(k)$ into n overlapping boxes of equal length n. In each box we fit the signal $y(k)$ using a poly mial function $y_n(k) = a_0 + a_1 x(k) + a_2 x^2(k) + ... + a_s x^s(k)$, where $x(k)$ is the x coo nate corresponding to the kth signal point. We calculate the r.m.s. fluctuation funct $F(n) = \sqrt{\frac{1}{N_{max}} \sum_{k=1}^{N_{max}} [y(k) - y_n(k)]^2}$.

To prove the superposition rule, we first focus on one particular box along the sig In order to find the analytic expression of best fit in this box, we write

$$I(a_0, ..., a_s) = \sum_{k=1}^{n} [y(k) - (a_0 + ... + a_s x^s(k))]^2, \tag{1.}$$

where $a_m, m = 0, ..., s$ are the same for all points in this box. "Best fit" requires t $a_m, m = 0, ..., s$ satisfy

$$\frac{\partial I}{\partial a_m} = 0, m = 0, ... s \tag{1.}$$

Combining Eq. (1.25) with (1.26) we obtain $s + 1$ equations

$$y_m = a_0 t_{m0} + a_1 t_{m1} ... + a_s t_{ms}, m = 0, ..., s \tag{1.}$$

where

$$y_m = \sum_{k=1}^{n} y(k)x^m(k), t_{mj} = \sum_{k=1}^{n} x^{m+j}(k), j = 0, ..., s \qquad (1.28)$$

From Eqs. (1.27) we determine $a_0, a_1, .., a_s$.

For the signals f, g and $f + g$ after the integration, in each box we have

$$f_m = a_0 t_{m0} + a_1 t_{m1}... + a_s t_{ms}, m = 0, ..., s$$

$$g_m = a_0' t_{m0} + a_1' t_{m1}... + a_s' t_{ms}, m = 0, ..., s$$

$$(f + g)_m = a_0'' t_{m0} + a_1'' t_{m1}... + a_s'' t_{ms}, m = 0, ..., s \qquad (1.29)$$

where f_m, g_m and $(f + g)_m$ correspond to y_m in Eqs. (1.27).

Comparing the three groups of equations in Eqs. (1.29), we find that, when we add the first two groups together, the left side becomes $f_m + g_m = (f + g)_m$, which is precisely the left side of the third group of equations. Thus we find

$$a_m'' = a_m + a_m', m = 0, ..., s \qquad (1.30)$$

and for each point k in every box, the polynomial fits for the signals f, g and $f + g$ satisfy

$$(f + g)_n(k) = f_n(k) + g_n(k). \qquad (1.31)$$

This result can be extended to all boxes in the signals. For the signal $f + g$ we obtain

$$\begin{aligned} F_{f+g}^2 &= \frac{1}{N_{max}} \sum_{k=1}^{N_{max}} [f(k) - f_n(k)]^2 + [g(k) - g_n(k)]^2 \\ &\quad +2[f(k) - f_n(k)][g(k) - g_n(k)]. \end{aligned} \qquad (1.32)$$

After the substitutions $f(k) - f_n(k) = Y_f(k)$ and $g(k) - g_n(k) = Y_g(k)$, we rewrite the above equation as

$$\begin{aligned} F_{f+g}^2 &= \frac{1}{N_{max}} \Big[\sum_{k=1}^{N_{max}} (Y_f(k))^2 + \sum_{k=1}^{N_{max}} (Y_g(k))^2 \\ &\quad +2 \sum_{k=1}^{N_{max}} Y_f(k)Y_g(k) \Big] \\ &= F_f^2 + F_g^2 + \frac{2}{N_{max}} \sum_{k=1}^{N_{max}} Y_f(k)Y_g(k). \end{aligned} \qquad (1.33)$$

In the general case, we can utilize the Cauchy inequality

$$\left| \sum_{k=1}^{N_{max}} Y_f(k)Y_g(k) \right|$$

$$\leq \left(\sum_{k=1}^{N_{max}} (Y_f(k))^2 \right)^{1/2} \left(\sum_{k=1}^{N_{max}} (Y_g(k))^2 \right)^{1/2} \qquad (1.$$

and we find

$$(F_f - F_g)^2 \leq F_{f+g}^2 \leq (F_f + F_g)^2$$

$$\implies |F_f - F_g| \leq F_{f+g} \leq F_f + F_g. \qquad (1.$$

From Eqs. (1.27) for $m = 0$, in every box we have $\sum_{k=1}^{n} y(k) = \sum_{k=1}^{n} y_n(k)$. Thus we obt $\sum_{k=1}^{N_{max}} Y_f(k) = \sum_{k=1}^{N_{max}} Y_g(k) = 0$ where $Y_f(k)$ and $Y_g(k)$ fluctuate around zero. When Y_f and $Y_g(k)$ are not correlated, the value of the third term in Eq. (1.33) is close to zero we obtain the following superposition rule

$$F_{f+g}^2 = F_f^2 + F_g^2. \qquad (1.$$

1.8   Conclusion and Summary

In this section we consider different types of trends superposed on correlated noise, study how these trends affect the scaling behavior of the noise. We demonstrate t there is a competition between a trend and a noise, and that this competition can lea crossovers in the scaling. We investigate the features of these crossovers, their depende on the properties of the noise and the superposed trend. Surprisingly, we find that crosso which are a result of trends can exhibit power-law dependences on the parameters of trends. We show that these crossover phenomena can be explained by the superposit of the separate results of the DFA method on the noise and on the trend, assuming t the noise and the trend are not correlated, and that the scaling properties of the noise the apparent scaling behavior of the trend are known. Our work may provide some hel differentiate between different types of crossovers — e.g. crossovers which separate scal

regions with different correlation properties may differ from crossovers which are an artifact of trends. The results we present here could be useful for identifying the presence of trends and to accurately interpret correlation properties of noisy data.

Chapter 2

Effect of Nonstationarities on Detrended Fluctuation Analysis

2.1 Overview

Detrended fluctuation analysis (DFA) is a scaling analysis method used to quantify lo range power-law correlations in signals. Many physical and biological signals are "nois heterogeneous and exhibit different types of nonstationarities, which can affect the co lation properties of these signals. We systematically study the effects of three types nonstationarities often encountered in real data. Specifically, we consider nonstation sequences formed in three ways: (i) stitching together segments of data obtained fr discontinuous experimental recordings, or removing some noisy and unreliable parts fr continuous recordings and stitching together the remaining parts — a "cutting" proced commonly used in preparing data prior to signal analysis; (ii) adding to a signal with kno correlations a tunable concentration of random outliers or spikes with different amplitu and (iii) generating a signal comprised of segments with different properties — e.g. ferent standard deviations or different correlation exponents. We compare the differe between the scaling results obtained for stationary correlated signals and correlated sigr with these three types of nonstationarities. We find that introducing nonstationaritie stationary correlated signals leads to the appearance of crossovers in the scaling behav

and we study how the characteristics of these crossovers depend on: (a) the fraction and size of the parts cut out from the signal; (b) the concentration of spikes and their amplitudes; (c) the proportion between segments with different standard deviations or different correlations; and (d) the correlation properties of the stationary signal. We show how to develop strategies for pre-processing "raw" data prior to analysis, which will minimize the effects of nonstationarities on the scaling properties of the data and how to interpret the results of DFA for complex signals with different local characteristics.

2.2   Introduction to this chapter

In recent years, there has been growing evidence indicating that many physical and biological systems have no characteristic length scale and exhibit long-range power-law correlations. Traditional approaches such as the power-spectrum and correlation analysis are suited to quantify correlations in stationary signals [65, 66]. However, many signals which are outputs of complex physical and biological systems are nonstationary — the mean, standard deviation and higher moments, or the correlation functions are not invariant under time translation [65, 66]. Nonstationarity, an important aspect of complex variability, can often be associated with different trends in the signal or heterogeneous segments (patches) with different local statistical properties. To address this problem, detrended fluctuation analysis (DFA) was developed to accurately quantify long-range power-law correlations embedded in a nonstationary time series [1, 4]. This method provides a single quantitative parameter — the scaling exponent α — to quantify the correlation properties of a signal. One advantage of the DFA method is that it allows the detection of long-range power-law correlations in noisy signals with embedded polynomial trends that can mask the true correlations in the fluctuations of a signal. The DFA method has been successfully applied to research fields such as DNA [1–3, 17, 24–29, 67–69], cardiac dynamics [5–16, 18–23, 70–72], human gait [73], meteorology [48], climate temperature fluctuations [56, 57, 59], river flow and discharge [49, 50], neural receptors in biological systems [74], and economics [35–47]. The DFA method may also help identify different states of the same system with different scaling

behavior — e.g., the scaling exponent α for heart-beat intervals is different for healthy and sick individuals [14, 16] as well as for waking and sleeping states [10, 21].

To understand the intrinsic dynamics of a given system, it is important to analyze and correctly interpret its output signals. One of the common challenges is that the scaling exponent is not always constant (independent of scale) and crossovers often exist — i.e., the value of the scaling exponent α differs for different ranges of scales [5, 10, 16, 75, 76]. A crossover is usually due to a change in the correlation properties of the signal at different time or space scales, though it can also be a result of nonstationarities in the signal. A recent work considered different types of nonstationarities associated with different trends (e.g., polynomial, sinusoidal and power-law trends) and systematically studied their effect on the scaling behavior of long-range correlated signals [62]. Here we consider the effect of three other types of nonstationarities which are often encountered in real data or result from "standard" data pre-processing approaches.

(i) Signals with segments removed

First we consider a type of nonstationarity caused by discontinuities in signals. Discontinuities may arise from the nature of experimental recordings – e.g., stock exchange data are not recorded during the nights, weekends and holidays [35–42]. Alternatively, discontinuities may be caused by the fact that some noisy and unreliable portions of continuous recordings must be discarded, as often occurs when analyzing physiological signals [5–16, 18–23, 70–72]. In this case, a common pre–processing procedure is to cut out the noisy, unreliable parts of the recording and stitch together the remaining informative segments before any statistical analysis is performed. One immediate problem is how such cutting procedure will affect the scaling properties of long-range correlated signals. A careful consideration should be given when interpreting results obtained from scaling analysis, so that an accurate estimate of the true correlation properties of the original signal may be obtained.

(ii) Signals with random spikes

A second type of nonstationarity is due to the existence of spikes in data, which is very common in real life signals [5–16,18–23,70–73]. Spikes may arise from external conditions which have little to do with the intrinsic dynamics of the system. In this case, we must distinguish the spikes from normal intrinsic fluctuations in the system's output and filter them out when we attempt to quantify correlations. Alternatively, spikes may arise from the intrinsic dynamics of the system, rather than being an epiphenomenon of external conditions. In this second case, careful considerations should be given as to whether the spikes should be filtered out when estimating correlations in the signal, since such "intrinsic" spikes may be related to the properties of the noisy fluctuations. Here, we consider only the simpler case – namely, when the spikes are independent of the fluctuations in the signal. The problem is how spikes affect the scaling behavior of correlated signals, e.g., what kind of crossovers they may possibly cause. We also demonstrate to what extent features of the crossovers depend on the statistical properties of the spikes. Furthermore, we show how to recognize if a crossover indeed indicates a transition from one type of underlying correlations to a different type, or if the crossover is due to spikes without any transition in the dynamical properties of the fluctuations.

(*iii*) *Signals with different local behavior*

A third type of nonstationarity is associated with the presence of segments in a signal which exhibit different local statistical properties, e.g., different local standard deviations or different local correlations. Some examples include: (a) 24 hour records of heart rate fluctuations are characterized by segments with larger standard deviation during stress and physical activity and segments with smaller standard deviation during rest [6]; (b) studies of DNA show that coding and non-coding regions are characterized by different types of correlations [3, 67]; (c) brain wave analysis of different sleep stages (rapid eye movement [REM] sleep, light sleep and deep sleep) indicates that the signal during each stage may have different correlation properties [77]; (d) heartbeat signals during different sleep stages exhibit different scaling properties [21]. For such complex signals, results from scaling anal-

ysis often reveal a very complicated structure. It is a challenge to quantify the correlat properties of these signals. Here, we take a first step toward understanding the scal behavior of such signals.

We study these three types of nonstationarities embedded in correlated signals. apply the DFA method to stationary correlated signals and identical signals with artifici imposed nonstationarities, and compare the difference in the scaling results. (*i*) We that cutting segments from a signal and stitching together the remaining parts does affect the scaling for positively correlated signals. However, this cutting procedure stro affects anti-correlated signals, leading to a crossover from an anti-correlated regime small scales) to an uncorrelated regime (at large scales). (*ii*) For the correlated sig with superposed random spikes, we find that the scaling behavior is a superposition of scaling of the signal and the apparent scaling of the spikes. We analytically prove superposition relation by introducing a *superposition rule*. (*iii*) For the case of comp signals comprised of segments with different local properties, we find that their scal behavior is a superposition of the scaling of the different components — each compon containing only the segments exhibiting identical statistical properties. Thus, to obtain scaling properties of the signal, we need only to examine the properties of each compon — a much simpler task than analyzing the original signal.

The layout of the section is as follows: In Sec. 2.3, we describe how we use DFA metho quantify nonstationary signals. In Sec. 2.4, we compare the scaling properties of correla signals before and after removing some segments from the signals. In Sec. 2.5, we consi the effect of random spikes on correlated signals. In Sec. 2.6, we study signals comprise segments with different local behavior. We systematically examine all resulting crossov their conditions of existence, and their typical characteristics associated with the differ types of nonstationarity. We summarize our findings in Sec. 2.7.

2.3   Method

We use DFA method $[1, 2]$ to quantify the correlation properties of nonstationary signals. For details see Sec. 1.3.

We note that for anti-correlated signals, the scaling exponent obtained from the DFA method overestimates the true correlations at small scales [62]. To avoid this problem, one needs first to integrate the original anti-correlated signal and then apply the DFA method [62]. The correct scaling exponent can thus be obtained from the relation between n and $F(n)/n$ [instead of $F(n)$]. In the following sections, we first integrate the signals under consideration, then apply DFA-2 to remove linear trends in these integrated signals. In order to provide a more accurate estimate of $F(n)$, the largest box size n we use is $N_{max}/10$, where N_{max} is the total number of points in the signal.

We compare the results of the DFA method obtained from the nonstationary signals with those obtained from the stationary signal $u(i)$ and examine how the scaling properties of a detrended fluctuation function $F(n)$ change when introducing different types of nonstationarities.

2.4   Removing and stitching together remaining segments

In this section, we study the effect of nonstationarity caused by removing segments of a given length from a signal and stitching together the remaining parts — a "cutting" procedure often used in pre-processing data prior to analysis. To address this question, we first generate a stationary correlated signal $u(i)$ (see Sec. 1.3) of length N_{max} and a scaling exponent α, using the modified Fourier filtering method [61]. Next, we divide this signal into N_{max}/W non-overlapping segments of size W and randomly remove some of these segments. Finally, we stitch together the remaining segments in the signal $u(i)$ [Fig. 2.1(a)], thus obtaining a surrogate nonstationary signal which is characterized by three parameters: the scaling exponent α, the segment size W and the fraction of the signal $u(i)$, which is removed.
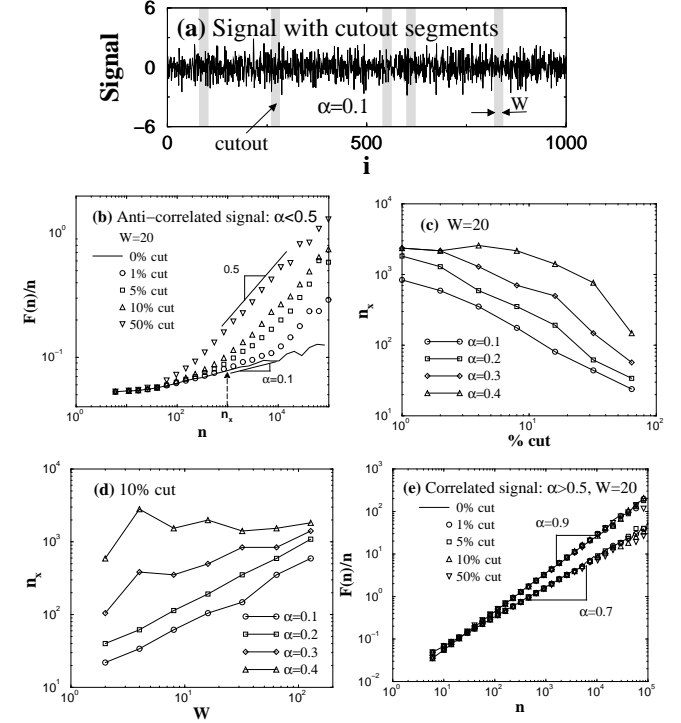
Figure 2.1: Effects of the "cutting" procedure on the scaling behavior of stationary correlated signals.

$N_{max} = 2^{20}$ is the number of points in the signals (standard deviation $\sigma = 1$) and W the size of the cutout segments. (a) A stationary signal with 10% of the points removed. The removed parts are presented by shaded segments of size $W = 20$ and the remaining parts are stitched together. (b) Scaling behavior of nonstationary signals obtained from anti-correlated stationary signal (scaling exponent $\alpha < 0.5$) after the cutting procedure: crossover from anti-correlated to uncorrelated ($\alpha = 0.5$) behavior appears at scale $n_\times$. The crossover scale $n_\times$ decreases with increasing the fraction of points removed from the signal. Dependence of the crossover scale $n_\times$ on the fraction (c) and on the size W (d) of cutout segments for anti-correlated signals with different scaling exponent α. (e) Cutting procedure applied to correlated signals ($\alpha > 0.5$).

We find that the scaling behavior of such a nonstationary signal strongly depends on the scaling exponent α of the original stationary correlated signal $u(i)$. As illustrated in Fig. 2.1(b), for a stationary *anti-correlated* signal with $\alpha = 0.1$, the cutting procedure causes a crossover in the scaling behavior of the resultant nonstationary signal. This crossover appears even when only 1% of the segments are cut out. At the scales larger than the crossover scale $n_\times$ the r.m.s. fluctuation function behaves as $F(n) \sim n^{0.5}$, which means an uncorrelated randomness, i.e., the anti-correlation has been completely destroyed in this regime. For all anti-correlated signals with exponent $\alpha < 0.5$, we observe a similar crossover behavior. This result is surprising, since researchers often take for granted that a cutting procedure before analysis does not change the scaling properties of the original signal. Our simulation shows that this assumption is not true, at least for anti-correlated signals.

Next, we investigate how the two parameters — the segment size W and the fraction of points cut out from the signal — control the effect of the cutting procedure on the scaling behavior of anti-correlated signals. For the fixed size of the segments ($W = 20$), we find that the crossover scale $n_\times$ *decreases* with *increasing* the fraction of the cutout segments [Fig. 2.1(c)]. Furthermore, for anti-correlated signals with small values of the scaling exponent α, e.g., $\alpha = 0.1$ and $\alpha = 0.2$, we find that $n_\times$ and the fraction of the cutout segments display an approximate power-law relationship. For a fixed fraction of the removed segments, we find that the crossover scale $n_\times$ *increases* with *increasing* the segment size W [Fig. 2.1(d)]. To minimize the effect of the cutting procedure on the correlation properties, it is advantageous to cut smaller number of segments of larger size W. Moreover, if the segments which need to be removed are too close (e.g., at a distance shorter than the size of the segments), it may be advantageous to cut out both the segments and a part of the signal between them. This will effectively increase the size of the segment W without substantially changing the fraction of the signal which is cut out, leading to an increase in the crossover scale $n_\times$. Such strategy would minimize the effect of this type of nonstationarity on the scaling properties of data. For small values of the scaling exponent α ($\alpha < 0.25$), we find that $n_\times$ and W follow power-law relationships [Fig. 2.1(d)]. The reason

we do not observe a power-law relationship between $n_\times$ and W and between $n_\times$ and fraction of cutout segments for the values of the scaling exponent α close to 0.5 may be to the fact that the crossover regime becomes broader when it separates scaling regions w similar exponents, thus leading to uncertainty in defining $n_\times$. For a fixed W and a fixed fraction of the removed segments [see Figs. 2.1(c) and (d)], we observe that $n_\times$ increase with the increasing value of the scaling exponent α, i.e., the effect of the cutting proced on the scaling behavior decreases when the anti-correlations in the signal are weaker closer to 0.5).

Finally, we consider the case of correlated signals $u(i)$ with $1.5 > \alpha > 0.5$. Surprisin we find that the scaling of correlated signals is not affected by the cutting procedure. observation remains true independently of the segment size W — from very small W up to very large $W = 5000$ segments — even when up to 50% of the segments are remo from a signal with $N_{max} \sim 10^6$ points [Fig. 2.1(e)].

2.5 Random Outliers or Spikes

In this section, we consider nonstationarity related to the presence of random spikes in d and we study the effect of this type of nonstationarity on the scaling properties of correla signals. First, we generate surrogate nonstationary signals by adding random spikes t stationary correlated signal $u(i)$ [see Sec. 1.3 and Fig. 2.2(a-c)].

We find that the correlation properties of the nonstationary signal with spikes depe on the scaling exponent α of the stationary signal and the scaling exponent α_{sp} of the spi When uncorrelated spikes ($\alpha_{sp} = 0.5$) are added to a correlated or anti-correlated station signal [Fig 2.2(d) and (e)], we observe a change in the scaling behavior with a crosso at a characteristic scale $n_\times$. For anti-correlated signals ($\alpha < 0.5$) with random spikes, find that at scales smaller than $n_\times$, the scaling behavior is close to the one observed the stationary anti-correlated signal without spikes, while for scales larger than $n_\times$, th is a crossover to random behavior. In the case of correlated signals ($\alpha > 0.5$) with rand spikes, we find a different crossover from uncorrelated behavior at small scales, to correla
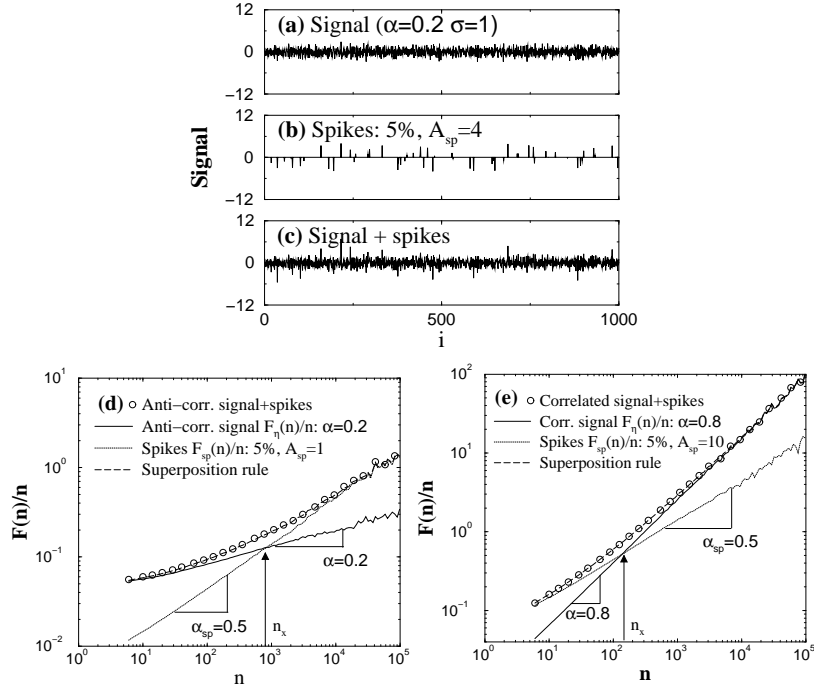
Figure 2.2: Effects of random spikes on the scaling behavior of stationary correlated signals. (a) An example of an anti-correlated signal $u(i)$ with scaling exponent $\alpha = 0.2$, $N_{max} = 2^{20}$ and standard deviation $\sigma = 1$. (b) A series of uncorrelated spikes ($\alpha_{sp} = 0.5$) at 5% randomly chosen positions (concentration $p = 0.05$) and with uniformly distributed amplitudes A_{sp} in the interval $[-4, 4]$. (c) The superposition of the signals in (a) and (b). (d) Scaling behavior of an anti-correlated signal $u(i)$ ($\alpha = 0.2$) with spikes ($A_{sp} = 1$, $p = 0.05$, $\alpha_{sp} = 0.5$). (e) Scaling behavior of a correlated signal $u(i)$ ($\alpha = 0.8$) with spikes ($A_{sp} = 10$, $p = 0.05$, $\alpha_{sp} = 0.5$).

behavior at large scales with an exponent close to the exponent of the original stationary correlated signal. Moreover, we find that spikes with a very small amplitude can cause strong crossovers in the case of anti-correlated signals, while for correlated signals, identical

concentrations of spikes with a much larger amplitude do not affect the scaling. Based these findings, we conclude that uncorrelated spikes with a sufficiently large amplitude affect the DFA results at large scales for signals with $\alpha < 0.5$ and at small scales for sig with $\alpha > 0.5$.

To better understand the origin of this crossover behavior, we first study the scal of the spikes only [see Fig. 2.2(b)]. By varying the concentration p ($0 \leq p \leq 1$) and amplitude A_{sp} of the spikes in the signal, we find that for the general case when the spi may be correlated, the r.m.s. fluctuation function behaves as

$$F_{sp}(n)/n = k_0\sqrt{p}A_{sp}n^{\alpha_{sp}},$$

where k_0 is a constant and α_{sp} is the scaling exponent of the spikes.

Next, we investigate the analytical relation between the DFA results obtained fr the original correlated signal, the spikes and the superposition of signal and spikes. Si the original signal and the spikes are not correlated, we can use a *superposition rule* (Sec. 1.7.1) to derive the r.m.s. fluctuation function $F(n)/n$ for the correlated signal w spikes:

$$[F(n)/n]^2 = [F_\eta(n)/n]^2 + [F_{sp}(n)/n]^2,$$

where $F_\eta(n)/n$ and $F_{sp}(n)/n$ are the r.m.s. fluctuation function for the signal and the spil respectively. To confirm this theoretical result, we calculate $\sqrt{[F_\eta(n)/n]^2 + [F_{sp}(n)/n]^2}$ Figs. 2.2(d), (e)] and find this Eq. (2.2) is remarkably consistent with our experimen observations.

Using the superposition rule, we can also theoretically predict the crossover scale $n_\times$ the intercept between $F_\eta(n)/n$ and $F_{sp}(n)/n$, i.e., where $F_\eta(n_\times) = F_{sp}(n_\times)$. We find th

$$n_\times = \left(\sqrt{p}A_{sp}\frac{k_0}{b_0}\right)^{1/(\alpha-\alpha_{sp})},$$

since the r.m.s. fluctuation function for the signal and the spikes are $F_\eta(n)/n = b_0n^\alpha$ and $F_{sp}(n)/n = k_0\sqrt{p}A_{sp}n^{\alpha_{sp}}$ [Eq. (2.1)], respectively. This result predicts the position the crossover depending on the parameters defining the signal and the spikes.

Our result derived from the superposition rule can be useful to distinguish two cases: (*i*) the correlated stationary signal and the spikes are independent (e.g., the case when a correlated signal results from the intrinsic dynamics of the system while the spikes are due to external perturbations); and (*ii*) the correlated stationary signal and the spikes are dependent (e.g., both the signal and the spikes arise from the intrinsic dynamics of the system). In the latter case, the identity in the superposition rule is not correct (see Sec. 1.7.1).

2.6   Signals comprised of segments with different properties

Next, we study the effect of nonstationarities on complex patchy signals where different segments show different local behavior. This type of nonstationarity is very common in real world data [3, 6, 21, 67, 77]. Our discussion of signals composed of only two types of segments is limited to two simple cases: (A) different standard deviations and (B) different correlations.

2.6.1   Signals with different local standard deviations

Here we consider nonstationary signals comprised of segments with the same local scaling exponent, but different local standard deviations. We first generate a stationary correlated signal $u(i)$ (see Sec. 1.3) with fixed standard deviation $\sigma_1 = 1$. Next, we divide the signal $u(i)$ into non-overlapping segments of size W. We then randomly choose a fraction p of the segments and amplify the standard deviation of the signal in these segments, $\sigma_2 = 4$ [Fig.2.3(a)]. Finally, we normalize the entire signal to global standard deviation $\sigma = 1$ by dividing the value of each point of the signal by $\sqrt{(1-p)\sigma_1^2 + p\sigma_2^2}$.

For nonstationary *anti-correlated* signals ($\alpha < 0.5$) with segments characterized by two different values of the standard deviation, we observe a crossover at scale $n_\times$ [Fig.2.3(b)]. For small scales $n < n_\times$, the behavior is anti-correlated with an exponent equal to the scaling exponent α of the original stationary anti-correlated signal $u(i)$. For large scales $n > n_\times$, we find a transition to random behavior with exponent 0.5, indicating that the
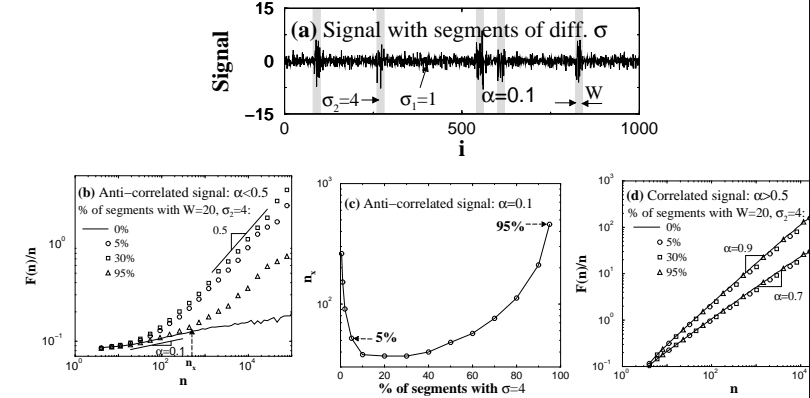
Figure 2.3: Scaling behavior of nonstationary correlated signals with different local standard deviation.
(a) Anti-correlated signal ($\alpha = 0.1$) with standard deviation $\sigma_1 = 1$ and amplified segments with standard deviation $\sigma_2 = 4$. The size of each segment is $W = 20$ and the fraction the amplified segments is $p = 0.1$ from the total length of the signal ($N_{max} = 2^{20}$). Scaling behavior of the signal in (a) for a different fraction p of the amplified segments (after normalization of the globe standard deviation to unity). (c) Dependence of the crossover scale $n_\times$ on the fraction p of amplified segments for the signal in (a). (d) Scaling behavior of nonstationary signals obtained from correlated stationary signals ($1 > \alpha > 0.5$) with standard deviation $\sigma_1 = 1$, for a different fraction of the amplified segments with $\sigma_2 = 4$;

anti-correlations have been destroyed. The dependence of crossover scale $n_\times$ on the fraction p of segments with larger standard deviation is shown in Fig. 2.3(c). The dependence is monotonic because for $p = 0$ and $p = 1$, the local standard deviation is constant throughout the signal, i.e., the signal becomes stationary and thus there is no crossover. Note asymmetry in the value of $n_\times$ — a much smaller value of $n_\times$ for $p = 0.05$ compared $p = 0.95$ [see Fig. 2.3(b-c)]. This result indicates that very few segments with a large standard deviation (compared to the rest of the signal) can have a strong effect on anti-correlations in the signal. Surprisingly, the same fraction of segments with a small standard deviation (compared to the rest of the signal) does not affect the anti-correlation

up to relatively large scales.

For nonstationary *correlated* signals ($\alpha > 0.5$) with segments characterized by two different values of the standard deviation, we surprisingly find no difference in the scaling of $F(n)/n$, compared to the stationary correlated signals with constant standard deviation [Fig. 2.3(d)]. Moreover, this observation remains valid for different sizes of the segments W and for different values of the fraction p of segments with larger standard deviation. We note that in the limiting case of very large values of σ_2/σ_1, when the values of the signal in the segments with standard deviation σ_1 could be considered close to "zero", the results in Fig. 2.3(d) do not hold and we observe a scaling behavior similar to that of the signal in Fig. 2.4(c) (see following section).

2.6.2 Signals with different local correlations

Next we consider nonstationary signals which consist of segments with identical standard deviation ($\sigma = 1$) but different correlations. We obtain such signals using the following procedure: (1) we generate two stationary signals $u_1(i)$ and $u_2(i)$ (see Sec. 1.3) of identical length N_{max} and with different correlations, characterized by scaling exponents α_1 and α_2; (2) we divide the signals $u_1(i)$ and $u_2(i)$ into non-overlapping segments of size W; (3) we randomly replace a fraction p of the segments in signal $u_1(i)$ with the corresponding segments of $u_2(i)$. In Fig. 2.4(a), we show an example of such a complex nonstationary signal with different local correlations. In this Section, we study the behavior of the r.m.s. fluctuation function $F(n)/n$. We also investigate $F(n)/n$ separately for each component of the nonstationary signal (which consists only of the segments with identical local correlations) and suggest an approach, based on the DFA results, to recognize such complex structures in real data.

In Fig. 2.4(d), we present the DFA result on such a nonstationary signal, composed of segments with two different types of local correlations characterized by exponents $\alpha_1 = 0.1$ and $\alpha_2 = 0.9$. We find that at small scales, the slope of $F(n)/n$ is close to α_1 and at large scales, the slope approaches α_2 with a bump in the intermediate scale regime. This is not
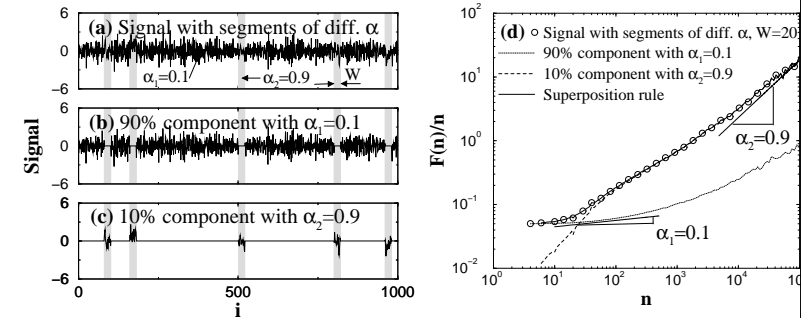

Figure 2.4: Scaling behavior of a nonstationary signal with two different scaling exponents. (a) Nonstationary signal (length $N_{max} = 2^{20}$, standard deviation $\sigma = 1$) which is a mixture of correlated segments with exponent $\alpha_1 = 0.1$ (90% of the signal) and segments with exponent $\alpha_2 = 0.9$ (10% of the signal). The segment size is $W = 20$; (b) the 90% component containing all segments with $\alpha_1 = 0.1$ and the remaining segments (with $\alpha_2 = 0.9$) replaced by zero; (c) the 10% component containing all segments with $\alpha_2 = 0.9$ and the remaining segments (with $\alpha_1 = 0.1$) are replaced by zero; (d) DFA results for the mixed signal in (a), for the individual components in (b) and (c), and our prediction obtained from the superposition rule.

surprising, since $\alpha_1 < \alpha_2$ and thus $F(n)/n$ is bound to have a small slope (α_1) at small scales and a large slope (α_2) at large scales. However, it is surprising that although 90% of the signal consists of segments with scaling exponent α_1, $F(n)/n$ deviates at small scales ($n \approx 10$) from the behavior expected for an anti-correlated signal $u(i)$ with exponent α_1 [see, e.g., the solid line in Fig. 2.1(b)]. This suggests that the behavior of $F(n)/n$ for a nonstationary signal comprised of mixed segments with different correlations is dominated by the segments exhibiting higher positive correlations even in the case when their relative fraction in the signal is small. This observation is pertinent to real data such as: (*i*) heart rate recordings during sleep where different segments corresponding to different sleep stages exhibit different types of correlations [21]; (*ii*) DNA sequences including coding and noncoding regions characterized by different correlations [3, 67, 69] and (*iii*) brain wave signals

during different sleep stages [77].

To better understand the complex behavior of $F(n)/n$ for such nonstationary signals, we study their components separately. Each component is composed only of those segments in the original signal which are characterized by identical correlations, while the segments with different correlations are substituted with zeros [see Figs. 2.4(b) and (c)]. Since the two components of the nonstationary signal in Fig. 2.4(a) are independent, based on the superposition rule [Eq. (2.2)], we expect that the r.m.s. fluctuation function $F(n)/n$ will behave as $\sqrt{[F_1(n)/n]^2 + [F_2(n)/n]^2}$, where $F_1(n)/n$ and $F_2(n)/n$ are the r.m.s. fluctuation functions of the components in Fig. 2.4(b) and Fig. 2.4(c), respectively. We find a remarkable agreement between the superposition rule prediction and the result of the DFA method obtained directly from the mixed signal [Fig 2.4(d)]. This finding helps us understand the relation between the scaling behavior of the mixed nonstationary signal and its components.

Information on the effect of such parameters as the scaling exponents α_1 and α_2, the size of the segments W and their relative fraction p on the scaling behavior of the components provides insight into the scaling behavior of the original mixed signal. When the original signal comes from real data, its composition is *a priori* unknown. A first step is to "guess" the type of correlations (exponents α_1 and α_2) present in the signal, based on the scaling behavior of $F(n)/n$ at small and large scales [Fig 2.4(d)]. A second step is to determine the parameters W and p for each component by matching the scaling result from the superposition rule with the original signal. Hence in the following subsections, we focus on the scaling properties of the components and how they change with p, α and W.

Dependence on the fraction of segments

First, we study how the correlation properties of the components depend on the fraction p of the segments with identical local correlations.

For components containing segments with anti-correlations ($0 < \alpha < 0.5$) and fixed size W [Fig. 2.4(b)], we find a crossover to random behavior ($\alpha = 0.5$) at large scales, which becomes more pronounced (shift to smaller scales) when the fraction p decreases
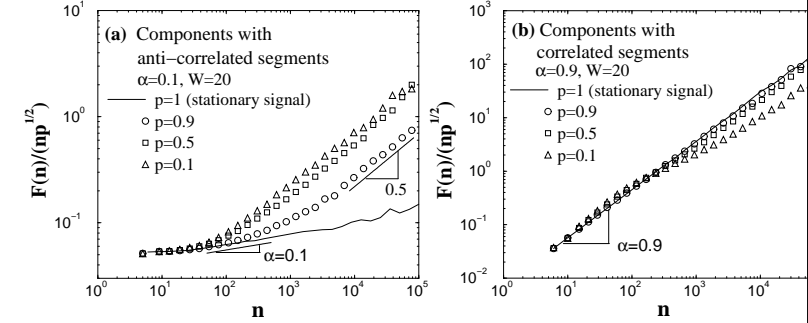

Figure 2.5: Dependence of the scaling behavior of components on the fraction p of segments with identical local correlations, emphasizing data collapse at small scales. The segment size is $W = 20$ and the length of the components is $N_{max} = 2^{20}$. (a) Components containing anti-correlated segments ($\alpha = 0.1$), at small scales ($n \leq W$). The slope of $F(n)/n$ is identical to that expected for a stationary ($p = 1$) signal with the same anti-correlations. After rescaling $F(n)/n$ by $\sqrt{p}$, at small scales all curves collapse on the curve for the stationary anti-correlated signal. (b) Components containing correlated segments ($\alpha = 0.9$), at small scales ($n \leq W$). The slope of $F(n)/n$ is identical to that expected for a stationary ($p = 1$) signal with the same correlations. After rescaling $F(n)/n$ by $\sqrt{p}$, at small scales all curves collapse on the curve for the stationary correlated signal.

[Fig. 2.5(a)]. At *small* scales ($n \leq W$), the slope of $F(n)/n$ is identical to that expected for a stationary signal $u(i)$ (i.e., $p = 1$) with the same anti-correlations [solid line in Fig. 2.5(a)]. Moreover, we observe a vertical shift in $F(n)/n$ to lower values when the fraction p of non-zero anti-correlated segments decreases. We find that at small scales after rescaling $F(n)/n$ by $\sqrt{p}$, all curves collapse on the curve for the stationary anti-correlated signal $u(i)$ [Fig. 2.5(a)]. Since at small scales ($n \leq W$) the behavior of $F(n)/n$ does not depend on the segment size W, this collapse indicates that the vertical shift in $F(n)/n$ is due only to the fraction p. Thus, to determine the fraction p of anti-correlated segments in a nonstationary signal [mixture of anti-correlated and correlated segments, Fig. 2.4(a)], we only need to estimate at small scales the vertical shift in $F(n)/n$ between the mixed signal

53

[Fig. 2.4(d)] and a stationary signal $u(i)$ with identical anti-correlations. This approach is valid for nonstationary signals where the fraction p of the anti-correlated segments is much larger than the fraction of the correlated segments in the mixed signal [Fig. 2.4(a)], since only under this condition the anti-correlated segments can dominate $F(n)/n$ of the mixed signal at small scales [Fig. 2.4(d)].

For components containing segments with positive correlations $(0.5 < \alpha < 1)$ and fixed size W [Fig. 2.4(c)], we observe a similar behavior for $F(n)/n$, with collapse at *small* scales $(n \leq W)$ after rescaling by $\sqrt{p}$ [Fig. 2.5(b)] (For $\alpha > 1$, there are exceptions with different rescaling factors, see Fig. 2.7). At small scales the values of $F(n)/n$ for components containing segments with positive correlations are much larger compared to the values of $F(n)/n$ for components containing an identical fraction p of anti-correlated segments [Fig. 2.5(a)]. Thus, for a mixed signal where the fraction of correlated segments is not too small (e.g., $p \geq 0.2$), the contribution at small scales of the anti-correlated segments to $F(n)/n$ of the mixed signal [Fig. 2.4(d)] may not be observed, and the behavior (values and slope) of $F(n)/n$ will be dominated by the correlated segments. In this case, we must consider the behavior of $F(n)/n$ of the mixed signal at large scales only, since the contribution of the anti-correlated segments at large scales is negligible. Hence, we next study the scaling behavior of components with correlated segments at *large* scales.

For components containing segments with positive correlations and fixed size W [Fig. 2.4(c)], we find that at *large* scales the slope of $F(n)/n$ is identical to that expected for a stationary signal $u(i)$ (i.e., $p = 1$) with the same correlations [solid line in Fig. 2.6(a)]. We also observe a vertical shift in $F(n)/n$ to lower values when the fraction p of non-zero correlated segments in the component decreases. We find that after rescaling $F(n)/n$ by p, at large scales all curves collapse on the curve representing the stationary correlated signal $u(i)$ [Fig. 2.6(a)]. Since at large scales $(n \gg W)$, the effect of the zero segments of size W on the r.m.s. fluctuation function $F(n)/n$ for components with correlated segments is negligible, even when the zero segments are 50% of the component [see Fig. 2.6(a)], the finding of a collapse at large scales indicates that the vertical shift in $F(n)/n$ is only due to the fraction

p of the correlated segments. Thus, to determine the fraction p of correlated segments in a nonstationary signal (which is a mixture of anti-correlated and correlated segments [Fig. 2.4(a)]), we only need to estimate at large scales the vertical shift in $F(n)/n$ between the mixed signal [Fig. 2.4(d)] and a stationary signal $u(i)$ with identical correlations.
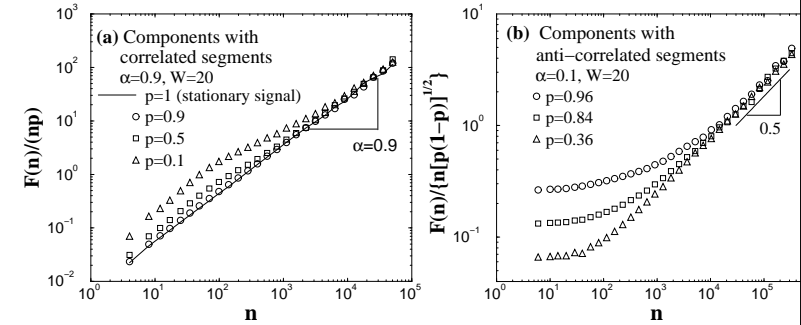

Figure 2.6: Dependence of scaling behavior of components on the fraction p of the segments with identical local correlations, emphasizing data collapse at *large* scales. The segment size is $W = 20$ and the length of the components is $N_{max} = 2^{20}$. (a) Components containing correlated segments ($\alpha = 0.9$), at *large* scales ($n \gg W$). The slope of $F(n)/n$ is identical to that expected for a stationary ($p = 1$) signal with the same correlations. After rescaling $F(n)/n$ by p, at large scales all curves collapse on the curve for the stationary correlated signal. (b) Components containing anti-correlated segments ($\alpha = 0.1$) at *large* scales ($n \gg W$). There is a crossover to random behavior ($\alpha = 0.5$). After rescaling $F(n)/n$ by $\sqrt{p(1-p)}$, all curves collapse at large scales.

For components containing segments with anti-correlations and fixed size W [Fig. 2.4(c)], we find that at large scales in order to collapse the $F(n)/n$ curves ($n \gg W$) [Fig. 2.5(b)], we need to rescale $F(n)/n$ by $\sqrt{p(1-p)}$ [see Fig. 2.6(b)]. Note that there is a difference between the rescaling factors for components with anti-correlated and correlated segments at small [Figs. 2.5(a-b)] and large [Figs. 2.6(a-b)] scales. We also note that for components with correlated segments ($\alpha > 0.5$) and sufficiently small p, there is a different rescaling factor of $\sqrt{p(1-p)}$ in the intermediate scale regime [see Fig. 2.7].

For components containing segments of white noise ($\alpha = 0.5$), we find no change in the scaling exponent as a function of the fraction p of the segments, i.e., $\alpha = 0.5$ for the components at both small and large scales. However, we observe at all scales a vertical shift in $F(n)/n$ to lower values with decreasing p: $F(n)/n \sim \sqrt{p}$.

Strongly correlated segments

For components containing segments with stronger positive correlations ($\alpha > 1$) and fixed $W = 20$, we find that at small scales ($n < W$), the slope of $F(n)/n$ does not depend on the fraction p and is close to that expected for a stationary signal $u(i)$ with identical correlations (Fig. 2.7). Surprisingly we find that in order to collapse the $F(n)/n$ curves obtained for different values of the fraction p, we need to rescale $F(n)/n$ by $\sqrt{p(1-p)}$ instead of $\sqrt{p}$, which is the rescaling factor at small scales for components containing segments with correlations $\alpha < 1$. Thus $\alpha = 1$ is a threshold indicating when the rescaling factor changes. Our simulations show that this threshold increases when the segment size W increases.

For components containing a sufficiently small fraction p of correlated segments ($\alpha > 0.5$), we find that in the intermediate scale regime there is a crossover to random behavior with slope 0.5. The $F(n)/n$ curves obtained for different values of p collapse in the intermediate scale regime if we rescale $F(n)/n$ by $\sqrt{p(1-p)}$ (Fig. 2.7). We note that this random behavior regime at intermediate scales shrinks with increasing the fraction p of correlated segments and, as expected, for p close to 1 this regime disappears (see the $p = 0.9$ curve in Fig. 2.7).

Dependence on the size of segments

Next, we study how the scaling behavior of the components depends on the size of the segments W.

First, we consider components containing segments with anti-correlations. For a fixed value of the fraction p of the segments, we study how $F(n)/n$ changes with W. At small scales, we observe a behavior with a slope similar to the one for a stationary signal $u(i)$ with
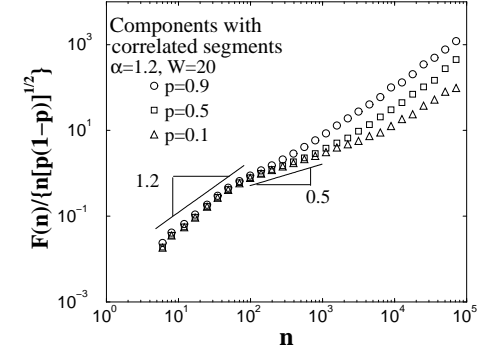

Figure 2.7: Dependence of the scaling behavior of components on the fraction p of segments with strong positive correlations ($\alpha = 1.2$).

The segment size is $W = 20$ and the length of the components is $N_{max} = 2^{20}$. A rescaling $F(n)/n$ by $\sqrt{p(1-p)}$, all curves collapse at small scales ($n < W$) with slope and at intermediate scales with slope 0.5. The intermediate scale regime shrinks whe increases.

identical anti-correlations [Fig. 2.8(a)]. At large scales, we observe a crossover to rand behavior (exponent $\alpha = 0.5$) with an increasing crossover scale when W increases. At la scales, we also find a vertical shift with increasing values for $F(n)/n$ when W decrea [Fig. 2.8(a)]. Moreover, we find that there is an equidistant vertical shift in $F(n)/n$ w W decreases by a factor of ten, suggesting a power-law relation between $F(n)/n$ and W large scales.

For components containing correlated segments with a fixed value of the fraction p find that in the intermediate scale regime, the segment size W plays an important rol the scaling behavior of $F(n)/n$ [Fig. 2.8(b)]. We first focus on the intermediate scale reg when both $p = 0.1$ and $W = 20$ are fixed [middle curve in Fig. 2.8(b)]. We find that fo small fraction p of the correlated segments, $F(n)/n$ has slope $\alpha = 0.5$, indicating rand behavior [Fig. 2.8(b)] which shrinks when p increases [see Fig. 2.7]. Thus, for compone containing correlated segments, $F(n)/n$ approximates at large and small scales the behav
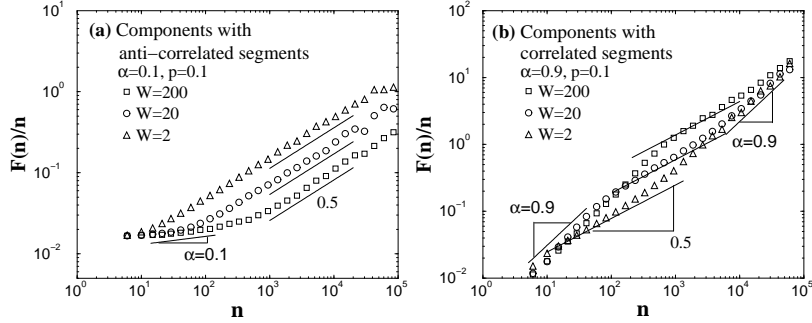
Figure 2.8: Dependence of the scaling behavior of components on the segment size W. The fraction $p = 0.1$ of the non-zero segments is fixed and the length of the components is $N_{max} = 2^{20}$. (a) Components containing anti-correlated segments ($\alpha = 0.1$). At large scales ($n \gg W$), there is a crossover to random behavior ($\alpha = 0.5$). An equidistant vertical shift in $F(n)/n$ when W decreases by a factor of ten suggests a power-law relation between $F(n)/n$ and W. (b) Components containing correlated segments ($\alpha = 0.9$). At intermediate scales, $F(n)/n$ has slope $\alpha = 0.5$, indicating random behavior. An equidistant vertical shift in $F(n)/n$ suggests a power-law relation between $F(n)/n$ and W.

of a stationary signal with identical correlations ($\alpha = 0.9$), while in the intermediate scale regime there is a plateau of random behavior due to the random "jumps" at the borders between the non-zero and zero segments [Fig. 2.4(c)]. Next, we consider the case when the fraction of correlated segments p is fixed while the segment size W changes. We find a vertical shift with increasing values for $F(n)/n$ when W increases [Fig. 2.8(b)], opposite to what we observe for components with anti-correlated segments [Fig. 2.8(a)]. Since the vertical shift in $F(n)/n$ is equidistant when W increases by a factor of ten, our finding indicates a power-law relationship between $F(n)/n$ and W.

Scaling Expressions

To better understand the complexity in the scaling behavior of components with correlated and anti-correlated segments at different scales, we employ the superposition rule (see 1.7.1).

For each component we have

$$F(n)/n = \sqrt{[F_{corr}(n)/n]^2 + [F_{rand}(n)/n]^2},$$

where $F_{corr}(n)/n$ accounts for the contribution of the correlated or anti-correlated non-zero segments, and $F_{rand}(n)/n$ accounts for the randomness due to "jumps" at the borders between non-zero and zero segments in the component.

i) Components with correlated segments ($\alpha > 0.5$)

At small scales $n < W$, our findings presented in Fig. 2.5(b) suggest that there is substantial contribution from $F_{rand}(n)/n$. Thus from Eq. (2.4),

$$F(n)/n \approx F_{corr}(n)/n \sim b_0 \sqrt{p} n^\alpha,$$

where $b_0 n^\alpha$ is the r.m.s. fluctuation function for stationary ($p = 1$) correlated signal [Eq. (1.9) and [62]].

Similarly, at large scales $n \gg W$, we find that the contribution of $F_{rand}(n)/n$ is negligible [see Fig. 2.6(a)], thus from Eq. (2.4) we have

$$F(n)/n \approx F_{corr}(n)/n \sim b_0 p n^\alpha.$$

However, in the intermediate scale regime, the contribution of $F_{rand}(n)/n$ to $F(n)/n$ is substantial. To confirm this we use the superposition rule [Eq. (2.4)] and our estimates of $F_{corr}(n)/n$ at small [Eq. (2.5)] and large [Eq. (2.6)] scales [We note that, for components containing strongly correlated segments (e.g., $\alpha = 1.2$ when $W = 20$, see Fig. 2.7), at small scales the contribution of the correlated non-zero segments [$F_{corr}(n)/n$] is still substantial; however, we have $F(n)/n \approx F_{corr}(n)/n \sim A\sqrt{p(1-p)}n^\alpha$]. The result we obtain from

$$F_{rand}(n)/n = \sqrt{[F(n)/n]^2 - [b_0 \sqrt{p} n^\alpha]^2 - [b_0 p n^\alpha]^2}$$

overlaps with $F(n)/n$ in the intermediate scale regime, exhibiting a slope of ≈ 0.5: $F_{rand}(n)/n \sim n^{0.5}$ [Fig. 2.9(a)]. Thus, $F_{rand}(n)/n$ is indeed a contribution due to the random jumps

between the non-zero correlated segments and the zero segments in the component [see Fig. 2.4(c)].

Further, our results in Fig. 2.8(b) suggest that in the intermediate scale regime $F(n)/n \sim W^{g_c(\alpha)}$ for fixed fraction p, where the power-law exponent $g_c(\alpha)$ may be a function of the scaling exponent α characterizing the correlations in the non-zero segments. Since at intermediate scales $F_{\rm rand}(n)/n$ dominates the scaling [Eq. (2.7) and Fig. 2.9(a)], from Eq. (2.4) we find $F_{\rm rand}(n)/n \approx F(n)/n \sim W^{g_c(\alpha)}$. We also find that at intermediate scales, $F(n)/n \sim \sqrt{p(1-p)}$ for fixed segment size W (see Fig. 2.7). Thus from Eq. (2.4) we find $F_{\rm rand}(n)/n \approx F(n)/n \sim \sqrt{p(1-p)}$. Hence we obtain the following general expression

$$F_{\rm rand}(n)/n \sim h(\alpha)\sqrt{p(1-p)}W^{g_c(\alpha)}n^{0.5}. \tag{2.8}$$

Here we assume that $F_{\rm rand}(n)/n$ also depends directly on the type of correlations in the segments through some function $h(\alpha)$.

To determine the form of $g_c(\alpha)$ in Eq. (2.8), we perform the following steps:

(a) We fix the values of p and α, and from Eq. (2.7) we calculate the value of $F_{\rm rand}(n)/n$ for two different values of the segment size W, e.g., we choose $W_1 = 400$ and $W_2 = 20$.

(b) From the expression in Eq. (2.8), at the same scale n in the intermediate scale regime we determine the ratio:

$$F_{\rm rand}(W_1)/F_{\rm rand}(W_2) = (W_1/W_2)^{g_c(\alpha)}. \tag{2.9}$$

(c) We plot $F_{\rm rand}(W_1)/F_{\rm rand}(W_2)$ vs. α on a linear-log scale [Fig. 2.9(b)]. From the graph and Eq. (2.9) we obtain the dependence

$$
g_c(\alpha) = \frac{\log[F_{\rm rand}(W_1)/F_{\rm rand}(W_2)]}{\log(W_1/W_2)}
$$
$$
= \begin{cases} C\alpha - C/2, & 0.5 \le \alpha \le 1 \\ 0.50, & \text{for } \alpha > 1, \end{cases} \tag{2.10}
$$

where $C = 0.87 \pm 0.06$. Note that $g_c(0.5) = 0$.

To determine if $F_{\rm rand}(n)/n$ depends on $h(\alpha)$ in Eq. (2.8), we perform the following steps:

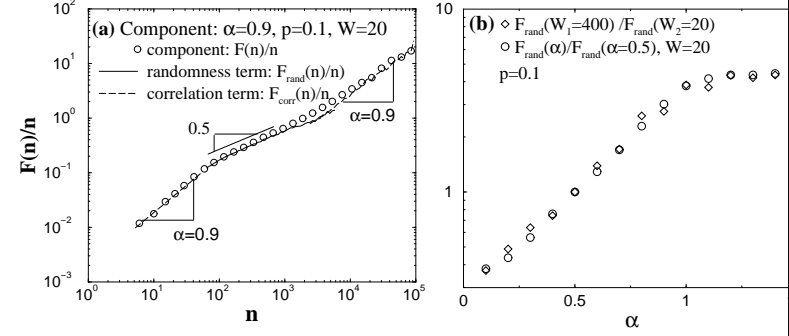(a) We fix the values of p and W and calculate the value of $F_{\rm rand}(n)/n$ for two different

Figure 2.9: Scaling behavior of components containing correlated segments ($\alpha > 0.5$). (a) $F(n)/n$ exhibits two crossovers and three scaling regimes at small, intermediate large scales. From the superposition rule [Eq. (2.4)] we find that the small and la scale regimes are controlled by the correlations ($\alpha = 0.9$) in the segments [$F_{\rm corr}(n)/n$ fr Eqs. (2.5) and (2.6)] while the intermediate regime [$F_{\rm rand}(n)/n \sim n^{0.5}$ from Eq. (2.7 dominated by the random jumps at the borders between non-zero and zero segments. The ratio $F_{\rm rand}(W_1 = 400)/F_{\rm rand}(W_2 = 20)$ in the intermediate scale regime for fixed p different values of α, and the ratio $F_{\rm rand}(\alpha)/F_{\rm rand}(\alpha = 0.5)$ for fixed p and $W = W_1/$ $F_{\rm rand}(n)/n$ is obtained from Eq. (2.7) and the ratios are estimated for all scales n in intermediate regime. The two curves overlap for a broad range of values for the expon α, suggesting that $F_{\rm rand}(n)/n$ does not depend on $h(\alpha)$ [see Eqs. (2.8) and (2.13)].

values of the scaling exponent α, e.g., 0.5 and any other value of α from Eq. (2.7).

(b) From the expression in Eq. (2.8), at the same scale n in the intermediate scale reg we determine the ratio:

$$\frac{F_{\rm rand}(\alpha)}{F_{\rm rand}(0.5)} = \frac{h(\alpha)}{h(0.5)}W^{g_c(\alpha)-g_c(0.5)} = \frac{h(\alpha)}{h(0.5)}W^{g_c(\alpha)}, \tag{2.}$$

since $g_c(0.5) = 0$ from Eq. (2.10).

(c) We plot $F_{\rm rand}(\alpha)/F_{\rm rand}(0.5)$ vs. α on a linear-log scale [Fig. 2.9(b)] and find that w $W \equiv W_1/W_2$ [in Eqs. (2.9) and (2.11)] this curve overlaps with $F_{\rm rand}(W_1)/F_{\rm rand}(W_2)$ vs [Fig. 2.9(b)] for all values of the scaling exponent $0.5 \le \alpha \le 1.5$. From this overlap

from Eqs. (2.9) and (2.11), we obtain

$$W^{g_c(\alpha)} = \frac{h(\alpha)}{h(0.5)} W^{g_c(\alpha)} \qquad (2.12)$$

for every value of α, suggesting that $h(\alpha) = const$ and thus $F_{\text{rand}}(n)/n$ can finally be expressed as:

$$F_{\text{rand}}(n)/n \sim \sqrt{p(1-p)} W^{g_c(\alpha)} n^{0.5}. \qquad (2.13)$$

ii) Components with anti-correlated segments ($\alpha < 0.5$)

Our results in Fig. 2.5(a) suggest that at small scales $n < W$ there is no substantial contribution of $F_{\text{rand}}(n)/n$ and that:

$$F(n)/n \approx F_{\text{corr}}(n)/n \sim b_0 \sqrt{p} n^{\alpha}, \qquad (2.14)$$

a behavior similar to the one we find for components with correlated segments [Eq. (2.5)].

In the intermediate and large scale regimes ($n \geq W$), from the plots in Fig. 2.6(b) and Fig. 2.8(a) we find the scaling behavior of $F(n)/n$ is controlled by $F_{\text{rand}}(n)/n$ and thus

$$F(n)/n \approx F_{\text{rand}}(n)/n \sim \sqrt{p(1-p)} W^{g_a(\alpha)} n^{0.5}, \qquad (2.15)$$

where $g_a(\alpha) = C\alpha - C/2$ for $0 < \alpha < 0.5$ [see Fig. 2.9(b)] and the relation for $F_{\text{rand}}(n)/n$ is obtained using the same procedure we followed for Eq. (2.13).

2.7   Conclusion

In this paper we studied the effects of three different types of nonstationarities using the DFA correlation analysis method. Specifically, we consider sequences formed in three ways: (*i*) stitching together segments of signals obtained from discontinuous experimental recordings, or removing some noisy and unreliable segments from continuous recordings and stitching together the remaining parts; (*ii*) adding random outliers or spikes to a signal with known correlations, and (*iii*) generating a signal composed of segments with different properties

— e.g. different standard deviations or different correlations. We compare the differe between the scaling results obtained for stationary correlated signals and for correla signals with artificially imposed nonstationarities.

(*i*) We find that removing segments from a signal and stitching together the remaining p does not affect the scaling behavior of positively correlated signals ($1.5 \geq \alpha > 0.5$), e when up to 50% of the points in these signals are removed. However, such a cutting pro dure strongly affects anti-correlated signals, leading to a crossover from an anti-correla regime (at small scales) to an uncorrelated regime (at large scales). The crossover scale increases with increasing value of the scaling exponent α for the original stationary a correlated signal. It also depends both on the segment size and the fraction of the po cut out from the signal: (1) $n_\times$ decreases with increasing fraction of cutout segments, (2) $n_\times$ increases with increasing segment size. Based on our findings, we propose an proach to minimize the effect of cutting procedure on the correlation properties of a sig When two segments which need to be removed are on distances shorter than the size of segment, it is advantageous to cut out both the segments and the part of the signal betw them.

(*ii*) Signals with superposed random spikes. We find that for an anti-correlated signal w superposed spikes at small scales, the scaling behavior is close to that of the stationary a correlated signal without spikes. At large scales, there is a crossover to random behav For a correlated signal with spikes, we find a different crossover from uncorrelated behav at small scales to correlated behavior at large scales with an exponent close to the expon of the original stationary signal. We also find that the spikes with identical density a amplitude may cause strong effect on the scaling of an anti-correlated signal while t have a much smaller or no effect on the scaling of a correlated signal — when the signals have the same standard deviations. We investigate the characteristics of the scal of the spikes only and find that the scaling behavior of the signal with random spike a superposition of the scaling of the signal and the scaling of the spikes. We analytic prove this superposition relation by introducing a *superposition rule*.

(*iii*) Signals composed of segments with different local properties. We find that

(a) For nonstationary correlated signals comprised of segments which are characterized by two different values of the standard deviation, there is no difference in the scaling behavior compared to stationary correlated signals with constant standard deviation. For nonstationary anti-correlated signals, we find a crossover at scale $n_\times$. For small scales $n < n_\times$, the scaling behavior is similar to that of the stationary anti-correlated signals with constant standard deviation. For large scales $n > n_\times$, there is a transition to random behavior. We also find that very few segments with large standard deviation can strongly affect the anti-correlations in the signal. In contrast, the same fraction of segments with standard deviation smaller than the standard deviation of the rest of the anti-correlated signal has much weaker effect on the scaling behavior — $n_\times$ is shifted to larger scales.

(b) For nonstationary signals consisting of segments with different correlations, the scaling behavior is a superposition of the scaling of the different components — where each component contains only the segments exhibiting identical correlations and the remaining segments are replaced by zero. Based on our findings, we propose an approach to identify the composition of such complex signals: A first step is to "guess" the type of correlations from the DFA results at small and large scales. A second step is to determine the parameters defining the components, such as the segment size and the fraction of non-zero segments. We studied how the scaling characteristics of the components depend on these parameters and provide analytic scaling expressions.

Part III

Statistical Physics Approaches to Physiological Signals

Chapter 3

Non-Random Fluctuations and Multi-scale Dynamics of Human Activity

3.1   Overview

We investigate if known extrinsic and intrinsic factors fully account for the complex features observed in recordings of human activity as measured from forearm motion in subjects undergoing their regular daily routine. We demonstrate that the apparently random forearm motion possesses dynamic patterns characterized by robust scale-invariant and nonlinear features. These patterns remain stable from one subject to another and are unaffected by changes in the average activity level that occur within individual subjects throughout the day and on different days of the week, since they persist during daily routine and when the same subjects undergo time-isolation laboratory experiments designed to account for the circadian phase and to control the known extrinsic factors. Further, by modeling the scheduled events imposed throughout the laboratory protocols, we demonstrate that they cannot account for the observed scaling patterns in activity fluctuations. We attribute these patterns to a previously unrecognized intrinsic nonlinear multi-scale control mechanism of human activity that is independent of known extrinsic factors such as random and scheduled

events, as well as the known intrinsic factors which possess a single characteristic time scale such as circadian and ultradian rhythms.

3.2   Introduction to this chapter

Control of human activity is complex, being influenced by many factors both extrinsic (work, recreation, reactions to unforeseen random events) and intrinsic (the circadian pacemaker that influences our sleep/wake cycle [78, 79] and ultradian oscillators with shorter time scales [80, 81]). The extrinsic factors may account for the apparently random fluctuations in human motion observed over short time scales while the intrinsic rhythms may account for the underlying regularity in average activity level over longer periods of up to 24 h. Further, human activity correlates with important physiological functions including whole body oxygen consumption and heart rate [10, 82–84].

3.3   Methods

Actiwatch devices are traditionally used to demarcate sleep versus wakefulness based on average activity levels, or to observe the mean pattern of activity as it changes across the day and night according to disease state (Fig. 3.1). The subject wears a wristwatch-sized *Actiwatch* recorder (Mini-Mitter Co., OR, USA) that unobtrusively measures changes in forearm acceleration in any plane (sensitive to $0.01g$, where g is the acceleration due to gravity) [85]. Each data point recorded in the device's internal memory represents the value of changes in acceleration sampled at 32 Hz and integrated over a 15-second epoch length. Recordings are made continuously for different experimental protocols over several weeks, yielding approximately 10^5 data points for each subject. Inhomogeneity of recording sensitivity across the range of activities is accounted for in the analyses.

Traditionally activity fluctuations are considered as random noise and have been ignored. We hypothesize that there are systematic patterns in the activity fluctuations that may be independent of known extrinsic and intrinsic factors. To test our hypotheses, we evaluate
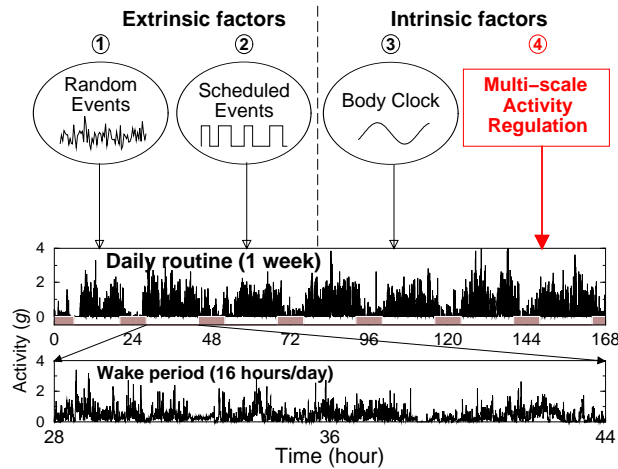
Figure 3.1: Independent contributors to the complex dynamics of human activity. Include: ① reaction to extrinsic random events, ② scheduled activities and, ③ intrinsic factors, notably the endogenous circadian pacemaker which influences the sleep/wake cycle. Our findings of scale-invariant activity patterns (Figs. 3.2-3.7) indicate a heretofore-unidentified intrinsic multi-scale control of human activity ④, which is independent of other extrinsic and intrinsic factors such as ①, ②, and ③. The second panel illustrates an actual one-week recording of human activity [85] during the daily routine protocol. Data structure highlights a 24-h sleep/wake periodic change in the mean activity — lowest during sleep (filled bars). The third panel, expanding a 16-h section of wakefulness, also shows patches of high and low average activity levels with apparent erratic fluctuations at various time scales. The bottom left panel is an activity recording from the same subject during the constant routine protocol with much lower average activity values compared to daily routine. The clear 2-h cycle is a result of scheduled laboratory events. The bottom right panel shows activity levels in the same subject during the forced desynchrony protocol, characterized by a 28-h sleep/wake cycle (as opposed to the 24-h rhythm in activity data during the daily routine).

structure of human activity during wakefulness, using: (i) probability distribution analy (ii) power spectrum analysis, and (iii) fractal scaling and nonlinear analysis. To elucidate presence of an intrinsic activity control center independent of known circadian, ultradi scheduled and random factors, we apply 3 complementary protocols.

• *Daily routine protocol*: We record activity data throughout two consecutive weeks 16 healthy ambulatory domiciliary subjects (8 males, 8 females, 19-44 years, mean 27 yea performing their routine daily activities. The only imposed constraints are that subjects to bed and arise at the same time each day (8 h sleep opportunity) and that they are permitted to have daytime naps (Fig. 3.1).

• *Constant routine protocol*: To assess intrinsic activity controllers (i.e. circadian other neural centers) independent of scheduled and random external influences, ac ity recordings are made in the laboratory throughout 38 h of constant posture (se recumbent), wakefulness, environment (21^oC, dim light [< 8 lux]), dietary intake a scheduled events [86, 87]. This protocol is performed in a subset of subjects (7 males females) that participated in the daily routine protocol. These highly controlled and c stant experimental conditions result in reduced average and variance of activity levels.

• *Forced desynchrony protocol*: To test for the presence of heretofore unidentified intri activity control centers, independent of known activity regulators (circadian pacemak while accounting for scheduled and random external influences, we employ the valida Forced desynchrony (FD) protocol [79]. Six (4 male, 2 female) of the 16 subjects t participated in the daily routine protocol completed the FD limb of the study. For ei days subjects remain in constant dim light (to avoid "resetting" the body clock). Sl periods are delayed by 4 h every day, such that subjects live on recurring 28 h "days", w all scheduled activities become desynchronized from the endogenous circadian pacema Thus, as measurements occur across all phases of the circadian clock, the effect of intri circadian influences can be removed [79]. Average activity level and activity variance also significantly reduced due to laboratory-imposed restrictions on the subjects activ (Fig. 3.1).

3.4 Results and discussion

When the same subject is studied in different protocols, we find large differences in the probability distributions (Fig. 3.2). For example, during wakefulness greater values of activity occur most frequently during the daily routine, intermediate activity values occur during the forced desynchrony, and the highest frequency of low activity values is seen during the constant routine (Fig. 3.2a). Indeed, the largest activity values encountered during the constant routine protocol are approximately two orders of magnitude less frequent than similar activity values encountered in the daily routine protocol. We find major differences between individuals in the distribution of activity values during the daily routine protocol (Fig. 3.2b). Such differences are expected given the different daily schedules, environments, and reactions to random events.

To test if the individual probability density curves follow a common functional form, we appropriately rescale the distributions of activity values on both axes to account for differences in average activity level and standard deviation while preserving the normalization to unit area. We divide the activity values by a constant, A_0, and multiply the probability density function by the same constant, where A_0 is the activity value before rescaling of each individual curve for which the cumulative probability (i.e., the area under the density function curve) is 60%. We find a remarkable similarity in the shapes of the probability distributions for each subject in all three protocols (Figs. 3.2a, e), and for all individuals when in the same protocol (Fig. 3.2f, g, h). The existence of a *universal* form of the probability distribution, independent of activity level in all individuals and in all protocols (Fig. 3.3a), suggests that a *common* underlying mechanism may account for the overall distribution of activity.

This probability distribution when plotted on a log-log scale reveals different characteristics above and below a distinct crossover point (Fig. 3.3a). At scales above the crossover activity level there is pronounced non-Gaussian tail (Fig. 3.3a). This tail on the log-log plot represents a power-law form, indicating an intrinsic self-similar structure for a range
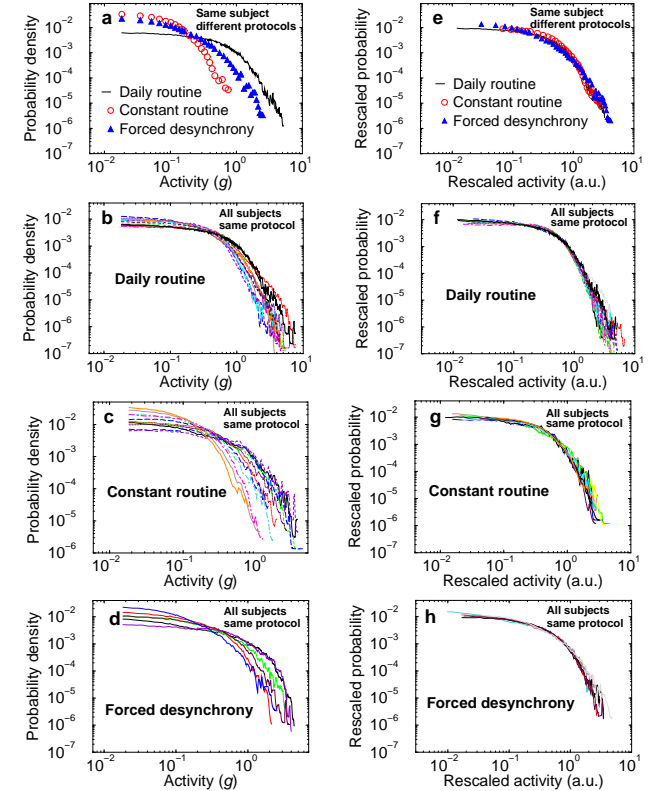
Figure 3.2: Common functional form for the probability distributions of activity values. (a) Probability distributions of activity values during wakefulness for an individual subject during 14 consecutive days of daily routine, 38 h of constant routine and 8 days of the forced desynchrony protocol. Probability distributions for all subjects during (b) the daily routine protocol, (c) the constant routine, and (d) the forced desynchrony protocol, indicate large difference between individuals. (e) – (h) Same probability distributions as in (a) – (d), after appropriately rescaling both axes. Data points for all subjects and for all three protocols collapse onto a single curve.

Figure 3.3: Group average of the rescaled distributions.
(a) During all three protocols. All distributions collapse onto a single curve, suggesting a common underlying mechanism of activity regulation. The same rescaling procedure as in Fig. 3.2 is used. (b) All individual distributions obtained for varied time windows during the daily routine.
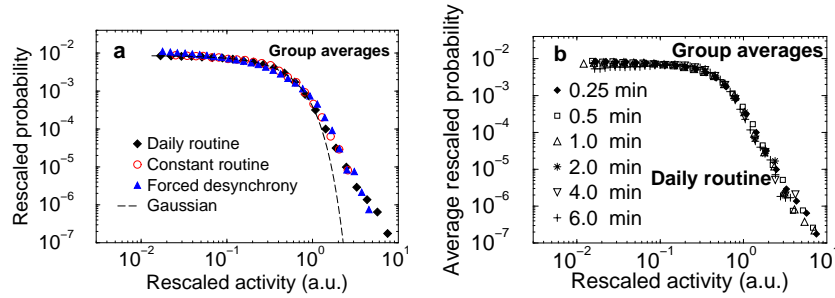
of activity values. Moreover, we find that the observed shape of the rescaled probability distribution remains unchanged when the data series are reanalyzed using a variety of observation windows ranging from 15 s to 6 min (Fig. 3.3b). This stability of the probability distribution over a range of time scales indicates that the underlying dynamic mechanisms controlling the activity have similar statistical properties on different time scales. Statistical self-similarity is a defining characteristic of fractal objects and is reminiscent of a wide class of physical systems with universal scaling properties. Our finding of a universal form of the probability distribution raises the possibility of an intrinsic mechanism that influences activity values in a self-similar "fractal" manner, that is unrelated to the individual's daily and weekly schedules, reactions to the environment, the average level of activity, the phase of the circadian pacemaker, and the time scale of observation.

We next perform power spectral analyses for all three protocols to determine whether there exist any systematic intrinsic ultradian rhythms of activity with periods of less than 24 h duration [80,88]. The data for each individual exhibit occasional peaks in the daily routine protocol for periods ranging from 30 min to 4 h. However, we find no systematic ultradian
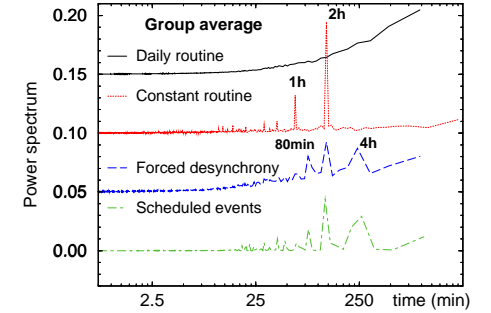

Figure 3.4: Group average power spectral densities for all three protocols.
Curves are vertically offset. Power spectra are shown with decreasing frequency from to right. Smooth behavior of the daily routine curve suggests absence of periodic rhyth in the ultradian range. The spectral density peaks for the simulated scheduled activ data representing controlled scheduled events during the protocol (bottom curve) ma the peaks observed in the original human activity data recorded during the forced des chrony protocol. Our analysis and simulation suggest that the observed peaks in the po spectrum are due to scheduled laboratory events and cannot be attributed to endogen ultradian rhythms.

rhythms within individuals from week to week, and no systematic ultradian rhythms in group average for the daily routine protocol (Fig. 3.4). The only systematic rhythms t are ostensibly in the ultradian range which emerge in the group data are at 4 h during forced desynchrony protocol (with harmonics at 2 h and 80 min) and at 2 h during constant routine protocol (with harmonics at 1 h and 30 min) (Fig. 3.1 and Fig. 3.4). Th peaks are caused by the controlled scheduled activities in the laboratory and are extrin to the body as they also occur in simulated scheduled activity data that assumes spec activity values for each scheduled behavior imposed throughout the laboratory protoc (Fig. 3.4). Thus, we find no evidence of systematic intrinsic ultradian rhythms in our da

To provide further insight into the dynamic control of activity, we next examine the te poral organization in the fluctuations in activity values. We perform detrended fluctuat

analysis (DFA) which quantifies correlations in the activity fluctuations after accounting for nonstationarity in the data by subtracting underlying polynomial trends [1, 2, 62, 89]. The DFA method quantifies the root mean square fluctuations, $F(n)$, of a signal at different time scales n. Power-law functional form, $F(n) \sim n^{\alpha}$, indicates self-similarity (fractal scaling). The parameter α, called the scaling exponent, quantifies the correlation properties in the signal: if $\alpha=0.5$, there is no correlation (random noise); if $\alpha < 0.5$, the signal is anticorrelated, where large activity values are more likely to be followed by small activity values; if $\alpha > 0.5$, there are positive correlations, where large activity values are more likely to be followed by large activity values (and vice versa for small activity values).
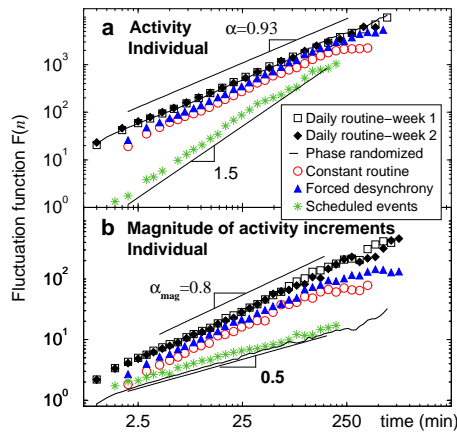

Figure 3.5: Long-range fractal correlations and nonlinearity in activity fluctuations. **(a)** DFA scaling of activity fluctuation for a subject during wakefulness, demonstrating strong positive correlations on time scales from seconds to hours. **(b)** DFA scaling of the magnitude series of activity increments for the same signals as in (a). A scaling exponent $\alpha_{\mathrm{mag}} \approx 0.8$ of similar value is observed for all three protocols, consistent with robust nonlinear dynamics.

Figure 3.5a shows that $F(n)$ for a typical subject during wakefulness exhibits a power-law

form over time scales from ≈ 1 min to ≈ 4 h. We find that the scaling exponent α is virtually identical for records obtained during the first week of daily routine ($\alpha = 0.92 \pm 0.04$, mean standard deviation among subjects), the second week ($\alpha = 0.92 \pm 0.06$) of the daily routine, the constant routine protocol ($\alpha = 0.88 \pm 0.05$), and the forced desynchrony protocol ($\alpha = 0.92 \pm 0.03$). The value of $\alpha \approx 0.9$ for all protocols and all individuals indicates that activity fluctuations are characterized by strong long-range positive correlations, and thus are not dominated by random factors. Furthermore, we find that this scaling behavior is not caused by the scheduled activities because simulated scheduled activity data that are generated by assigning a specific activity value for each scheduled event throughout the laboratory protocols yields an exponent of $\alpha = 1.5$ (Fig. 3.5a), which represents random-walk type behavior. These results suggest that the activity fluctuations are not a consequence of random events (in which case α would be 0.5) or scheduled events, but rather related to an underlying mechanism of activity control with stable fractal-like features over a wide range of time scales from minutes to hours. Since mean activity levels and the amplitude of the fluctuations are greatly reduced in the laboratory during the constant routine and forced desynchrony protocols (Fig. 3.1), we obtain smaller values of $F(n)$ (downward shift of the lines in Fig. 3.5a). However there is no change in the scaling exponent α. Similarly, the scaling exponents for the daily routine protocol are independent of the average activity levels of the different subjects (Fig. 3.6a), the mean activity level on different days of the week (Fig. 3.6b), and of the circadian phase, suggesting that this scaling pattern of activity fluctuations appears to be an intrinsic feature.

To test for the presence of nonlinear properties of the data, we analyze the "magnitude series" formed by taking the absolute values of the increments between consecutive activity values [23]. Again, from detrended fluctuation analysis of this series, we find practically identical scaling exponents, α_{mag}, for all three protocols, despite large differences in mean activity levels between protocols (Fig 3.5b). Moreover, all individuals have very similar values of the scaling exponent α_{mag} (Fig. 3.6a), which are not systematically changed by protocol. For the group, during the first week of daily routine, we find $\alpha_{\mathrm{mag}} = 0.78 \pm 0$
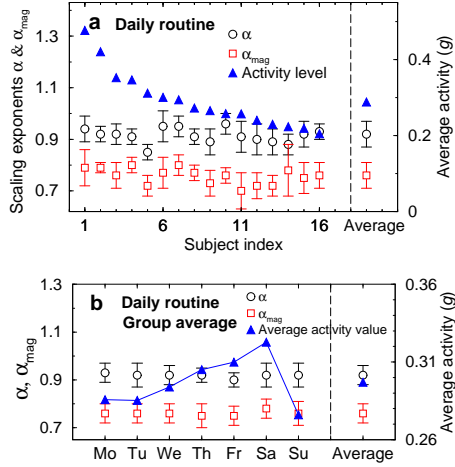
Figure 3.6: Stability of scaling and nonlinear features.
(a) Scaling exponents α and α_{mag} (left scale), and average activity levels (right scale) for all 16 subjects obtained from a 14-day daily routine protocol. Although the average activity level between subjects changes considerably (from 0.2 to 0.5), both scaling exponents are consistent for all subjects, exhibiting a group average of $\alpha = 0.92 \pm 0.05$ and $\alpha_{\mathrm{mag}} = 0.77 \pm 0.05$. **(b)** Group average scaling exponents α and α_{mag} calculated for different days of the week. While the average activity level progressively increases throughout the week (with a peak on Saturday and a minimum on Sunday), the group average scaling exponents α and α_{mag} remain practically constant, consistent with a robust underlying mechanism of control characterized by fractal and nonlinear features which do not change with activity level.

(mean $\pm$ standard deviation among subjects), during the second week $\alpha_{\mathrm{mag}} = 0.76 \pm 0.05$, during the constant routine protocol $\alpha_{\mathrm{mag}} = 0.82 \pm 0.05$, and during the forced desynchrony protocol $\alpha_{\mathrm{mag}} = 0.80 \pm 0.04$. Since $\alpha_{\mathrm{mag}} \approx 0.8 (> 0.5)$, there are positive long-range correlations in the magnitude series of activity increments, indicating the existence of nonlinear properties related to Fourier phase interactions (Fig. 3.5b) [23, 70]. To confirm that the observed positive correlations in the magnitude series indeed represent nonlinear features

in the activity data, we do the following test: we generate a surrogate time series by performing a Fourier transform on the activity recording from the same subject during daily routine as in Fig. 5a, preserving the Fourier amplitudes but randomizing the phases, and then performing an inverse Fourier transform. This procedure eliminates nonlinearities preserving only the linear features of the original activity recording such as the power spectrum and correlations. Thus, the new surrogate signal has the same scaling behavior with $\alpha = 0.93$ (Fig. 3.5a) as the original activity recording; however, it exhibits uncorrelated behavior for the magnitude series ($\alpha_{\mathrm{mag}} = 0.5$) (Fig. 3.5b). Our results show that the activity data contains important phase correlations which are canceled in the surrogate signal by the randomization of the Fourier phases, and that these correlations do not exist in the simulated scheduled activity. Further, our tests indicate that these nonlinear features are encoded in Fourier phase, suggesting an intrinsic *nonlinear* mechanism [70]. The similar value of α_{mag} for all three protocols and all individuals, which is different from $\alpha_{mag} = $ obtained for the simulated scheduled activity and for the phase randomized data, confirms that the intrinsic dynamics possess nonlinear features that are independent of the daily and weekly schedules, reaction to the environment, the average level of activity, and the phase of the circadian pacemaker.

To determine whether or not there is any alteration of the intrinsic patterns for dominant and non-dominant (left and right) hands [90], we record one week of activity data of the left and right hands simultaneously for five additional subjects in the daily protocol. all subjects, we find that the form of activity distribution (Fig. 3.7a) and the power-law correlations (Fig. 3.7b) are the same for dominant (more active) and non-dominant hands, confirming that the observed intrinsic patterns are independent of activity level.

Finally, to ensure that the power-law correlations are not an artifact produced by instrument, we obtain "test" activity data by attaching an *Actiwatch* to a 15 cm radius disk, turning at constant angular velocity of 45 rpm (Fig. 3.8a). The activity values of *Actiwatch* fluctuate only slightly, and analysis of these random fluctuations reveals scaling exponents $\alpha \approx 0.5$ and $\alpha_{\mathrm{mag}} \approx 0.5$ (Fig. 3.8b), which indicate random linear behavior
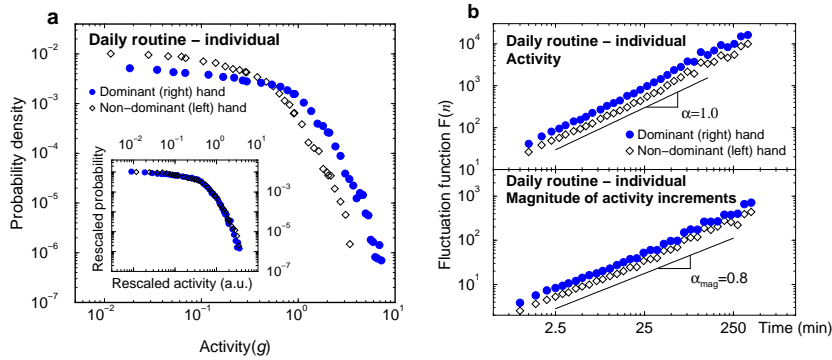
Figure 3.7: Comparison of left and right wrist activity.

(a) Distributions of left and right wrist activity for a typical subject. The subject is right-handed, and the activity level and variance of the right wrist is larger than that of the left wrist. As a result, compared to the left wrist, the right wrist has a smaller probability at small activity level, and a larger probability at large activity level. (b) DFA results of left and right wrist activity fluctuations reveal practically identical power-law correlations — the same value of α. The smaller values of $F(n)$ (vertical shift) for the left wrist are due to the smaller average activity level and variance of the left hand.

Thus, the stable values of α and α_{mag} observed in our subjects throughout the varied protocols do not depend on the recording device, but instead these exponents are inherent characteristics of the subjects, and that both hands have the same underlying dynamics of activity regulation.

3.5   Summary

In summary, the findings reported here offer insights into the mechanisms of human wrist activity control. Prior to our work, it has been a general belief, though never tested, that fluctuations in activity during wakefulness are somewhat random, influenced mainly by extrinsic factors such as reactions to unforeseen random events. Our findings of a stable form for the probability distribution, long-range power-law correlations and nonlinear Fourier-
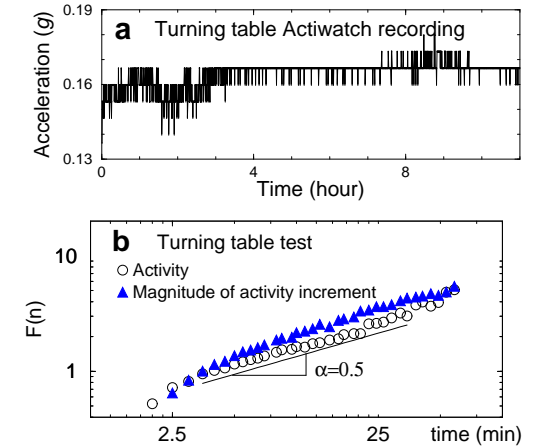

Figure 3.8: Turning table test for the *Actiwatch* device suggests the observed scaling featu in activity fluctuations are not an artifact of the device.

(a) Data recorded from an *Actiwatch* placed on a disk rotating with constant angular locity. (b) DFA correlation analysis of the fluctuations in (a) shows random noise behav in contrast to the strong positive correlations in activity fluctuations (Figs. 3.5, 3.7).

phase features on time scales from seconds to hours, and the consistency of our results am individuals and for different protocols, suggest that there exist previously unrecogni complex dynamic patterns of human activity that are unrelated to extrinsic factors or the average level of activity. We also show these scale-invariant patterns to be independ of known intrinsic factors related to the circadian and to any ultradian rhythms. Notably, these patterns are unchanged when obtained at different phases of the circadian pacema (ii) we do not observe systematic intrinsic ultradian rhythms in activity among subj in the daily routine experiment; (iii) imposing strong extrinsic ultradian rhythms at and 2 h in the laboratory protocols did not change the fractal scaling exponents α or α or the form of the probability distribution; and (iv) we find consistent results over a w range of time scales. Together, these findings strongly suggest that our results are n

reflection of the basic rest activity cycles or ultradian rhythms. We attribute these novel scale-invariant patterns to a robust *intrinsic multi-scale* mechanism of regulation (Fig. 3.1). Further, our findings suggest that activity control may be based on a multiple-component nonlinear feedback mechanism encompassing coupled neuronal nodes located both in the central and peripheral nervous systems, each acting in a specific range of time scales [91]. This insight provides key elements and guidance for future studies focused on modeling locomotor regulation [92, 93] .

Chapter 4

Synchronization Patterns in Cerebral Blood Flow and Peripheral Blood Pressure under Minor Stroke

4.1 Overview

Stroke is a leading cause of death and disability in the United States. The autoregulation of cerebral blood flow that adapts to changes in systemic blood pressure is impaired after stroke. We investigate blood flow velocities (BFV) from right and left middle cerebral arteries (MCA) and beat-to-beat blood pressure (BP) simultaneously measured from the finger, in 13 stroke and 11 healthy subjects using the mean value statistics and phase synchronization method. We find an increase in the vascular resistance and a much stronger cross-correlation with a time lag up to 20 seconds with the instantaneous phase increments of the BFV and BP signals for the subjects with stroke compared to healthy subjects.

4.2   Introduction to this chapter

Stroke is a leading cause of death and disability in people above certain age [94], yet many factors that set the stage for stroke and determine the outcome after stroke are not well understood.

Cerebral autoregulation involves several complex mechanisms maintaining steady blood flow to the brain in the presence of systemic blood pressure fluctuations. These mechanisms are impaired after an acute stroke and cerebral blood flow becomes dependent on blood pressure [95, 96]. Therefore, cerebral blood flow declines with falling blood pressure (which may lead to ischemia) and increases with rising blood pressure (which poses a risk of hemorrhage). Activities of daily living, such as rest and exercise, sitting and standing-up, even taking meals are associated with blood pressure fluctuations on a range of time scales. For example, standing-up may induce transient hypotension, which requires rapid cerebral vasodilatation to compensate for blood pressure decline and to maintain cerebral perfusion in the upright position [97]. This complex mechanisms of cerebral regulation is still not well understood. It is also not clear if cerebral autoregulation recovers after stroke [98]. Previous studies suggest that cerebral blood flow declines on the stroke side during orthostatic stress, posing a risk of reduced perfusion to the affected side of the brain [99].

Here we study the effects of stroke on cerebral autoregulation controlling the flow-pressure relationship. Our goal is to determine the effects of orthostatic stress on the dynamic relationship between blood flow velocities (BFV) in the middle cerebral arteries and the peripheral blood pressure (BP) from healthy subjects and patients with stroke. We find that the dynamics of flow-pressure regulation is impaired after a stroke and we determine indices allowing us to characterize and quantitate healthy cerebral autoregulation and its impairment after stroke.

4.3   Experimental design and data acquisition

4.3.1   Study groups

In our study we have:

- 13 patients (six male, seven female) with documented chronic ischemic minor str on MRI or CT (age 52.5 ± 7.3 years);

- 11 healthy subjects (age 47.2 ± 8.5 years).

4.3.2   Experimental protocol

All subjects participated in the following experimental protocol:

- Supine: subject rests in supine position for five minutes on the tilt table;

- Tilt: the table is moved upright to an 80 degree angle and the subject is in an upri position for five minutes;

- (Tilt) Hyperventilation: subject is asked to breathe quickly at approximately 1 Hz quency for three minutes in an upright position. Hyperventilation induces hypocap (reduced carbon dioxide), which is associated with vasoconstriction;

- (Tilt) CO2-rebreathing: The subject is asked to inhale deeply and hold the bre for one minute, then breathe a mixture of air and 5% CO_2 from rebreathing circ at a comfortable frequency for three minutes in an upright position. CO_2 rebrea ing increases carbon dioxide above normal levels and induces hypercapnia, which associated with vasodilatation.

4.3.3   Data acquisition

Blood flow velocity (BFV):
Transcranial Doppler ultrasonography system (MultiDop X4, Neuroscan, Inc.) is used monitoring BFV in both MCAs. The right and left MCA is insonated from the tempo

windows by placing the 2-MHz probe in the temporal area above the zygomatic arch. Each probe is positioned to record the maximal BFV and fixed at a desired angle using a three-dimensional positioning system attached to the light-metal probe holder. Special attention is given to stabilize the probes, since their steady position is crucial for continuous BFV recordings. Data are visually inspected and occasional extrasystoles and outlying values are removed using linear interpolation. A Fourier transform of the Doppler shift [a difference between the frequency of the emitted signal and its echo (frequency of reflected signal)] is used to calculate BFV. Systolic, diastolic, and mean BFV are detected from the envelope of MCA waveforms. A recent MRI study suggests that MCA diameter does not change during hyperventilation and breath-holding [100].

Blood pressure (BP):

Beat-to-beat BP is recorded from the finger with a Finapres device (Ohmeda Monitoring Systems, Englewood CO). With the finger positioned at the heart level and the temperature kept constant, this device can reliably track BP changes over a prolonged period of time [102].

BFV and BP signals are recorded simultaneously and the signal sampling frequency is 50 Hz.

4.4 Data

We first investigate the shape of BFV and BP signals for both healthy and stroke group during four experimental stages. The BFV waveform changes during vasoconstriction and vasodilation and therefore, we presume to be able to identify the subjects with impaired autoregulation.

In Fig. 4.1, we show examples of BFV signals from right and left MCA as well as BP signals from the finger during the tilt stage for one healthy subject and one stroke subject. For both subjects, right and left BFV signals and BP signals display a periodic behavior with a period of around one second, corresponding to heart frequency. Furthermore, for each subject, the shape of two BFV signals and one BP signal all look similar (especially
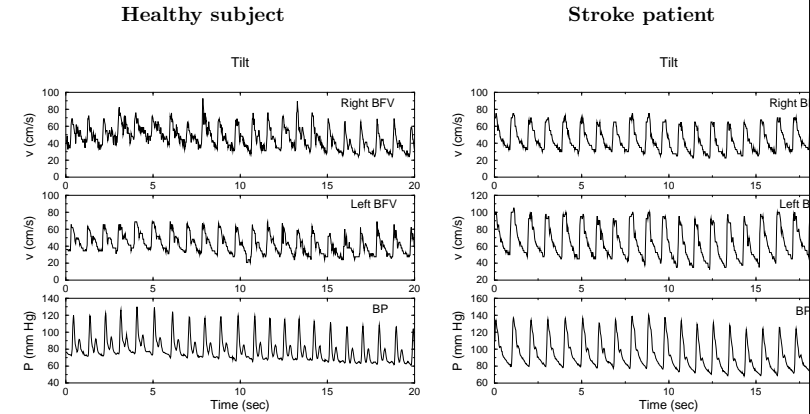

Figure 4.1: Right BFV, left BFV, and BP signals during tilt stage: (Left) One heal subject; (Right) One subject with stroke located in the right brain hemisphere.

BFV and BP signals have a similar shape and both are periodic signals with a period around one second, which reflects flow and pressure waveform during each heart beat. D from the stroke patient exhibit larger amplitude for the BFV signals and less pronoun second notch in the BP waveform.

for two BFV signals): a rapid increment of signals at the beginning of each circle and t a slow recovery in the rest of each circle. We also find some differences in the shape three signals between the two subjects shown in Fig. 4.1, however, we fail to find any gr differences in the shape of signals for the group of 13 stroke subjects and the group of healthy subjects. Therefore, such differences seem to be reflecting only trivial individ variability for different subjects. In summary, the shape of signals is not a good marker distinguishing stroke patients from healthy people.

In the next section, time domain analysis and synchronization techniques will be app to each subject to characterize two BFV signals and one BP signal.

4.5 Cerebral blood flow and peripheral blood pressure
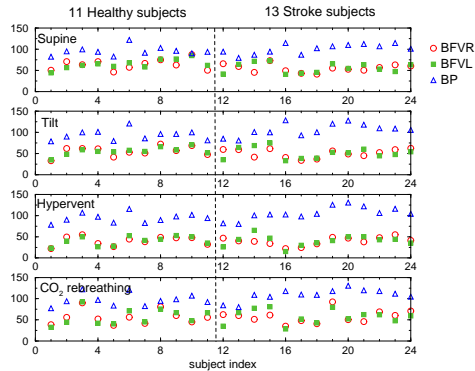
4.5.1 Time domain

Figure 4.2: Mean values of BFV and BP signals during four experimental stages for all 24 subjects in our database.

The x axis indicates the subject index, healthy subjects are to the left of vertical dash line and stroke patients are to the right. We find that in the tilt stage most stroke patients have relatively lower BFV. Note that increased relative difference between the BFV and BP mean values for the stroke patients compared to healthy subjects.

Several quantities have been used to quantify the properties of BFV and BP signals and the possible relations between them. For example, we have measured the magnitude of fluctuation (i.e., standard deviation) of BFV and BP signals for all subjects. From Fig. 4.1, one may infer that the signals for stroke patients have a larger standard deviation, and the BFV signals on the stroke side (e.g., right or left side in the brain) have a slightly smaller standard deviation compared to the normal side. However, in any of the four stages, we did not find any group differences for the standard deviation between these two groups. The different standard deviation between subjects seems to be more an indication of the individual variabilities in each subject than the indication of disease.

Instead, we find that the mean of signals in the tilt stage is a good quantity for de-

termining the differences between healthy and stroke groups. As shown in Fig. 4.2, find that in the tilt stage, most stroke patients have relatively lower BFV in MCA. M interesting, the exceptions, e.g., the 1st, 2nd, 4th, and the last stroke patients in Fig. are all female patients. Therefore, the mean of signals during tilt is a good marker for m stroke patients, but only a fair marker for female stroke patients. However, the relations between the stroke type, size and location and co-morbidities (e.g., hypertension) needs be examined before conclusions can be made about this gender effect.

Based on the results shown in Fig. 4.2, we further calculated the BP/BFV ratio of mean of signals for all subjects (see Fig. 4.3). In medical science, this ratio is often cal the vascular resistance — a parameter quantifying the elasticity of the arteries. Our resu suggest that the vascular resistance is increased after stroke. Vascular resistance seems provide a better quantitative distinction between healthy subjects and stroke subjects tl that from the mean of signals. As shown in Fig. 4.3, we find that during tilt, the ratio most healthy subjects are below the ratio = 2 line, while most the stroke patients rat are above the ratio = 2 line. These results suggest that stroke is associated with increa cerebrovascular resistance. Similar findings are also observed in supine position, but variability of inter-subjects observations is also greater compared to the tilt. Vascu resistance during hyperventilation and CO_2 rebreathing is similar between groups.

Our results, in some sense, suggest that cerebral autoregulation has been impaired chronic stroke patients. In healthy subjects, peripheral vascular resistance is increased w an upright position, but cerebral vascular resistance is not changed, due to autoregulati With impaired autoregulation after stroke, cerebral vessels react in a manner similar to peripheral vessels and vascular resistance is increased, which may result in reduced perfus during orthostatic stress.
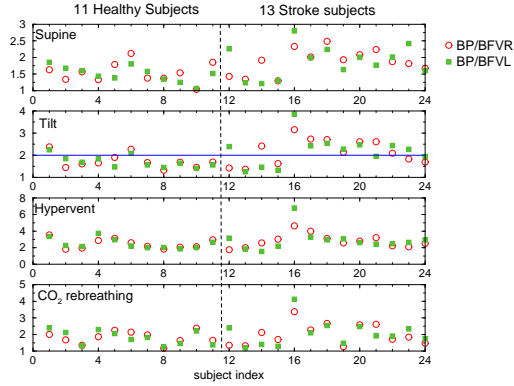
Figure 4.3: The ratio of the BFV and BP mean values (i.e., vascular resistance) during four stages for all 24 subjects in our database.

Note that during tilt, this ratio for most healthy subjects is below two (solid horizontal line), while most stroke patients exhibit a ratio above two. Similar increase in the vascular resistance is also observed in supine position.

4.6 Correlation between cerebral blood flow and peripheral blood pressure

Instantaneous phase synchronization technique

Our Synchronization algorithm is based on the Hilbert Transform. The Hilbert Transform of any signal $f(x)$ is defined as the following:

$$F(y) = \frac{1}{\pi}(\text{Cauchy Principal Value}) \int_{-\infty}^{\infty} \frac{f(x)}{x - y} dx. \qquad (4.1)$$

$F(y)$ has an apparent physical meaning in Fourier space: for any positive (negative) frequency ω, the Fourier component of $F(y)$ at ω is that of $f(x)$ at ω after a 90° clockwise (anti-clockwise) rotation in the complex number plane. For example, if the original signal is $\sin\alpha x$ ($\alpha > 0$), its Hilbert Transform will become $\cos\alpha y$.

Similar to the way we construct complex numbers, for any time series $s(t)$ we can always
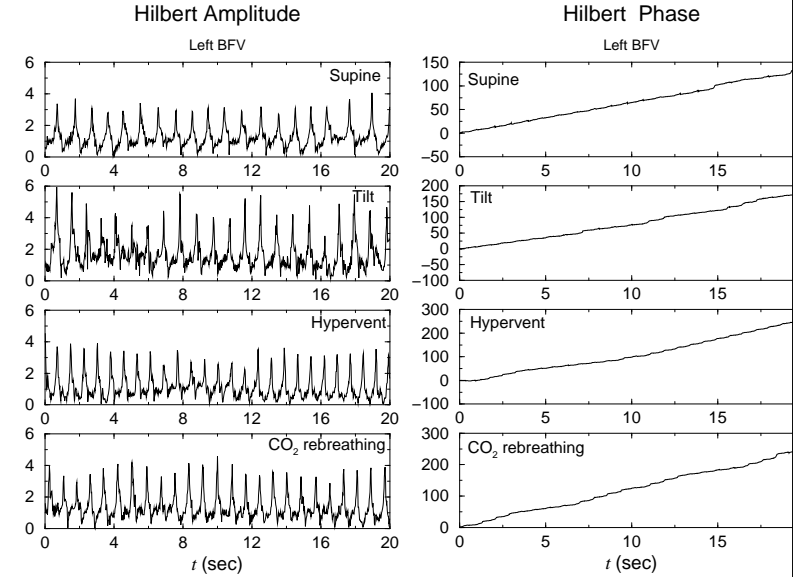

Figure 4.4: Instantaneous Hilbert amplitude (left) and Hilbert phase (right) of a filtered BFV signal from the left brain hemisphere (the filter is described in section 4.6) for a healthy subject, during four experimental stages.

The Hilbert phase exhibits complex fluctuations along strong linear trends. Simultaneous increase or decrease of the phase of the BFV and BP signals is an indication of synchronization behavior (see Fig. 4.4).

construct its "analytic signal" [103–107], which is defined as

$$s(t) + i\tilde{s}(t) = A(t)e^{i\phi(t)}, \qquad ($$

where $\tilde{s}(t)$ is the Hilbert Transform of $s(t)$. $A(t)$ and $\phi(t)$ are the Hilbert amplitude and phase of $s(t)$, respectively. Both the Hilbert amplitude and phase provide instantaneous attributes of a time series $s(t)$.

For a pure sinusoid, the Hilbert amplitude is constant and the Hilbert phase is a straight line over time. For more complex signals, both the Hilbert amplitude and phase may display complicated forms. As shown in Fig. 4.4, the Hilbert amplitude of the left BFV for a healthy

subject has a similar periodic behavior to that of the original signal, in all four experimental stages. The Hilbert phase of the left BFV of that subject during all four experimental stages can be looked upon as the superposition of a linear trend and additional fluctuations: the linear trend is trivial since it is caused by a periodic heart rate at a frequency of around 1 Hz; fluctuations are more important for us since they contain other useful information.

In practice, some filtering techniques are often needed before we calculate the Hilbert Transform of a time series. Actually, the value of analytic signals in Eqn. (4.2) can depend on the mean of $s(t)$, i.e., $s(t)$ and $s(t)+a$ (a is a constant) may have different Hilbert amplitude and phase, though both original signals have almost identical statistical properties. A simple way that may eliminate this effect is to subtract the mean of a time series before we calculate the Hilbert amplitude and phase. Due to similar reasons, the application of our algorithm on nonstationary signals is also limited, since the mean of a nonstationary signal is changing over time. To analyze a nonstationary signal, we often need to apply a Fourier high frequency pass filter first to remove the effect of the mean and slow drift of local mean in the signal before we calculate the Hilbert amplitude and phase.

Procedure

Our synchronization technique includes the following steps:

- First, we filter out low frequency trends in signals (high f pass filter $f > 0.05$ Hz is applied) and then normalize signals (let the standard deviation of signals $\sigma = 1$);

- Next, we calculate the Hilbert amplitude and phase of filtered signals;

- Last, we calculate the cross-correlation between the BFV and BP signals for both Hilbert amplitude and phase. Note that cross-correlation method will fail if original signals contain linear trends (trends will contribute to the results, but we are not interested in the effect of trends). To eliminate the linear trend in the Hilbert phase (see Fig. 4.4), we instead calculate the cross-correlation of the Hilbert phase increment of the BFV and BP signals.
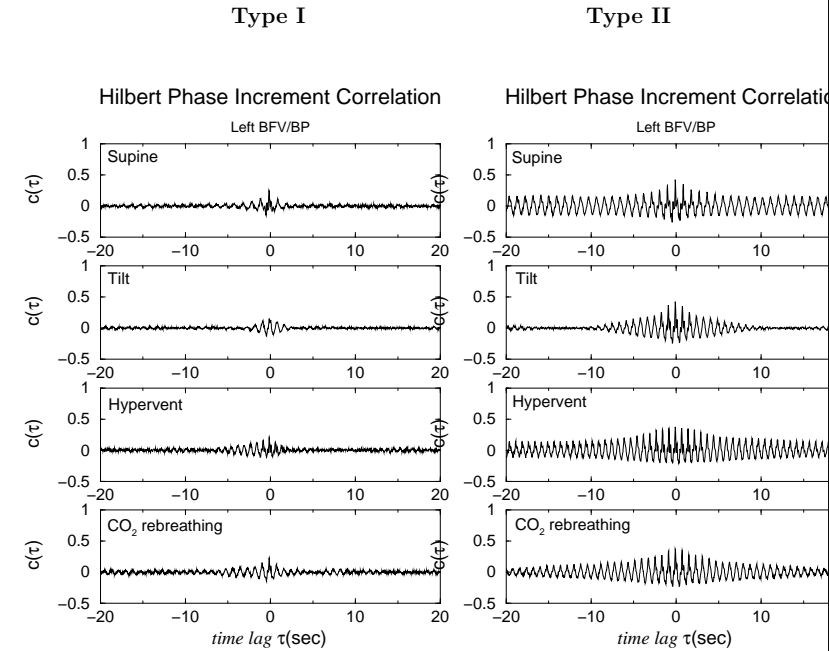

Figure 4.5: Cross-correlation function of the Hilbert phase increment for the BFV and [BP] signals during four experimental stages.

We find that all 24 subjects separate into two categories which exhibit two very disti[nct] types of behavior. **Type I** (Left): low-amplitude cross-correlations which decay at l[ags] $\approx$ 5sec., during all four stages. Most healthy subjects (eight out of eleven) belong [to] this type. **Type II** (Right): high-amplitude cross-correlations for lags up to 20 secon[ds] suggesting strong synchronization. Most stroke patients (eleven out of thirteen) belong [to] this type. We find that the stage where the best distinction from Type I correlation[s is] given varies for different subjects.

Results

The technique described in Section 4.6 has been applied to all 13 stroke patients and 11 healthy subjects. We find that, for the cross-correlation of both the Hilbert amplitude and the phase increment of BFV and BP signals, stroke patients display different behavior from that of healthy subjects. Furthermore, cross-correlation of the Hilbert phase increment often gives better results. In general, the cross-correlation results have the following two types:

- **Type I**: As shown in the left figure of Fig. 4.5, the BFV and BP signals have shorter correlation (less than 10 seconds). Most healthy subjects (eight out of eleven) and a few stroke patients (two out of thirteen) belong to this type. The stroke patients who belong to this type are both female;

- **Type II**: As shown in the right figure of Fig. 4.5, the BFV and BP signals have much longer sustained correlation (larger than 10 seconds). Most stroke patients (eleven out of thirteen) and a few healthy subjects (three out of eleven) belong to this type. The stage where the best distinction from **Type I** correlation is given varies for different subjects.

The short Type I correlations (less than 10 seconds) can usually be attributed to the effect of heart rate and/or respiration — i.e., it reflects the effect of other body regulations (similar to a kind of "background noise") on both BFV and BP signals and is beyond our interest. The longer Type II correlation, however, cannot be attributed to the effect of other regulations, instead, it may really reflect the functions of vascular tone. In other words, it may describe the true correlations between the BFV signals in MCA and peripheral BP signals. Therefore, the existence of such Type II correlations may indicate impaired cerebral autoregulation for those subjects.

4.7 Discussion

In our study we investigate blood flow velocity (BFV) signals measured from the right and left middle cerebral arteries (MCA) and peripheral blood pressure signals, from 11 healthy subjects and 13 subjects with documented minor stroke. We compare the properties of BFV and BP signals as well as synchronizations between BFV and BP signals for both groups. Based on our special experimental protocol, we evaluate the effect of minor chronic stroke on cerebral autoregulation and the effect of orthostatic stress on the relations between BFV and BP signals in the healthy subject and the stroke patient.

In time domain, we find that the standard deviation of BFV and BP signals during different stages is similar for healthy subjects and stroke patients. However, we find that healthy subjects and stroke patients have different responses to orthostatic stress, reflected by the mean BFV and BP values, as well as by the vascular resistance (mean BP/mean BFV ratio). We find that cerebral vascular resistance is increased in subjects with stroke, which suggests impaired autoregulation.

We also apply the synchronization method (based on the Hilbert transform) to quantify the possible phase relations between the BFV and BP signals. We find that the cross-correlations between the Hilbert phase increment of the BFV and BP signals provide reliable quantitative indices that clearly distinguish stroke patients from healthy subjects, even when the stroke is minor — a condition which is typically difficult to diagnose. These indices for stroke patients show a strong and sustained correlation between BFV and BP signals, which cannot be explained by heart rate and/or respiration. Such synchronization pattern is not apparent in healthy subjects and suggests impaired cerebral autoregulation for chronic stroke patients.

Using time domain analysis and the synchronization method, we are able to determine indices that can separate stroke patients from healthy subjects. These findings are clinically relevant and can be used to identify patients with impaired autoregulation who might be at risk of cerebral perfusion. They can be also used to distinguish patients with true

sient ischemic attacks who have reversible flow abnormalities from patients with permanent damage caused by the stroke.

Part IV

References

Bibliography

[1] C.-K. Peng, S.V. Buldyrev, S. Havlin, M. Simons, H.E. Stanley, A.L. Goldberger, Phys. Rev. E **49**, 1685 (1994).

[2] S. V. Buldyrev, A. L. Goldberger, S. Havlin, C.-K. Peng, H.E. Stanley, and M. Simons, Biophys. J. **65**, 2673 (1993).

[3] S.M. Ossadnik, S.B. Buldyrev, A.L. Goldberger, S. Havlin, R.N. Mantegna, C.-K. Peng, M. Simons, and H.E. Stanley, Biophys. J. **67**, 64 (1994).

[4] M.S. Taqqu, V. Teverovsky, and W. Willinger, Fractals **3** 785 (1995).

[5] N. Iyengar, C.-K. Peng, R. Morin, A. L. Goldberger, and L.A. Lipsitz, A.M. J. Physiol-Reg. I **40**, R1078 (1996).

[6] P. Ch. Ivanov, M.G. Rosenblum, C.-K. Peng, J.E. Mietus, S. Havlin, H.E. Stanley, and A.L. Goldberger, Nature **383**, 323 (1996).

[7] K.K.L. Ho, G.B. Moody, C.-K. Peng, J.E. Mietus, M.G. Larson, D. Levy, A.L. Goldberger, Circulation **96** 842 (1997).

[8] P. Ch. Ivanov, M.G. Rosenblum, C.-K. Peng, J.E. Mietus, S. Havlin, H.E. Stanley, and A.L. Goldberger, Physica A **249**, 587 (1998).

[9] M. Barbi, S. Chillemi, A. Di Garbo, R. Balocchi, C. Carpeggiani, M. Emdin, C. Michelassi, E. Santarcangelo, Chaos Solitions & Fractals **9**, 507 (1998).

[10] P. Ch. Ivanov, A. Bunde, L.A. Nunes Amaral, S. Havlin, J. Fritsch-Yelle, R. Baevsky, H.E. Stanley, and A.L. Goldberger, Europhysics Lett. **48**, 594 (1999).

[11] S.M. Pikkujamsa, T.H. Makikallio, L.B. Sourander, I.J. Raiha, P. Puukka, J. Sky, C.-K. Peng, A.L. Goldberger, H.V. Huikuri, Circulation **100**, 393 (1999).

[12] S. Havlin, S.V. Buldyrev, A. Bunde, A.L. Goldberger, P. Ch. Ivanov,C.-K. Peng, H.E. Stanley, Physica A **273**, 46 (1999).

[13] H.E. Stanley, L. Amaral, A.L. Goldberger, S. Havlin, P.C. Ivanov, and C.-K. Peng, Physica A **270**, 309 (1999).

[14] Y. Ashkenazy, M. Lewkowicz, J. Levitan, S. Havlin, K. Saermark, H. Moelgaard, P.E.B. Thomsen, Fractals **7**, 85 (1999).

[15] T. H. Makikallio, J. Koistinen, L. Jordaens, M.P. Tulppo, N. Wood, B. Golosarsky, C.-K. Peng, A.L. Goldberger, H.V. Huikuri, Am. J. Cardiol. **83**, 880 (1999).

[16] C.-K. Peng, S. Havlin, H.E. Stanley, and A.L. Goldberger, Chaos **5**, 82 (1995).

[17] S. Havlin, S.V. Buldyrev, A.L. Goldberger, S.M. Ossadniksm, C.-K. Peng, M. Simons, and H.E. Stanley, Chaos Soliton Fract. **6**, 171 (1995).

[18] P.A. Absil, R. Sepulchre, A. Bilge, and P. Gerard, Physica A **272**, 235 (1999).

[19] S. Havlin, L.A. Nunes Amaral, A.L. Goldberger, P.Ch. Ivanov, C.-K. Peng, and H.E. Stanley, Physica A **274**, 99 (1999).

[20] D. Toweill, K. Sonnenthal, B. Kimberly, S. Lai, and B. Goldstein, Crit. Care Med. **28**, 2051 (2000).

[21] A. Bunde, S. Havlin, J.W. Kantelhardt, T. Penzel, J.H. Peter, and K. Voigt, Phys. Rev. Lett. **85**, 3736 (2000).

[22] T.T. Laitio, H.V. Huikuri, E.S.H. Kentala, T.H. Makikallio, J.R. Jalonen, H. Helenius, K. Sariola-Heinonen, S. Yli-Mayry, and H. Scheinin, Anesthesiology **93**, 69 (2000).

[23] Y. Ashkenazy, P.Ch. Ivanov, S. Havlin, C.-K. Peng, A.L. Goldberger, and H.E. Stanley, Physical Rev. Lett. **86**, 1900 (2001).

[24] C.-K. Peng, S.V. Buldyrev, A.L. Goldberger, S. Havlin, M. Simons, and H.E. Stanley, Phys. Rev. E **47**, 3730 (1993).

[25] H.E. Stanley, S.V. Buldyrev, A.L. Goldberger, S. Havlin, R.N. Mantegna, C.-K. Peng, and M. Simons, Nuovo Cimento D **16**, 1339 (1994).

[26] R.N. Mantegna, S. V. Buldyrev, A.L. Goldberger, S. Havlin, C.-K. Peng, M. Simons, and H.E. Stanley, Phys. Rev. Lett. **73**, 3169 (1994).

[27] C.-K. Peng, S.V. Buldyrev, A.L. Goldberger, S. Havlin, R.N. Mantegna, M. Simons, and H.E. Stanley, Physica A **221**, 180 (1995).

[28] S. Havlin, S.V. Buldyrev, A.L. Goldberger, R.N. Mantegna, C.-K. Peng, M. Simons, and H.E. Stanley, Fractals **3**, 269 (1995).

[29] R.N. Mantegna, S. V. Buldyrev, A.L. Goldberger, S. Havlin, C.-K. Peng, M. Simons, and H.E. Stanley, Phys. Rev. Lett. **76**, 1979 (1996).

[30] S.V. Buldyrev, N.V. Dokholyan, A.L. Goldberger, S. Havlin, C.-K. Peng, H.E. Stanley, and G.M. Viswanathan, Physica A **249**, 430 (1998).

[31] S. Blesic, S. Milosevic, D. Stratimirovic, and M. Ljubisavljevic, Physica A **268**, 275 (1999).

[32] H. Yoshinaga, S. Miyazima, and S. Mitake, Physica A **280**, 582 (2000).

[33] C.A. Perazzo, E.A. Fernandez, D.R. Chialvo, and P.l. Willshaw, Fractal **8**, 279 (2000).

[34] Z. Siwy, S. Mercik, K. Ivanova and M. Ausloos (private communication).

[35] Y. Liu, P. Cizeau, M. Meyer, C.-K. Peng, and H.E. Stanley, Physica A **245**, 437 (1997).

[36] N. Vandewalle and M. Ausloos, Physica A **246**, 454 (1997).

[37] N. Vandewalle and M. Ausloos, Phy. Rev. E **58**, 6832 (1998).

[38] Y. Liu, P. Gopikrishnan, P. Cizeau, M. Meyer, C.-K. Peng, and H.E. Stanley, Phys. Rev. E **60**, 1390 (1999).

[39] I.M. Janosi, B. Janecsko, and I. Kondor, Physica A **269**, 111 (1999).

[40] M. Ausloos, N. Vandewalle, P. Boveroux, A. Minguet, and K. Ivanova, Physica A **274**, 229 (1999).

[41] M. Roberto, E. Scalas, G. Cuniberti, M. Riani, Physica A **269**, 148 (1999).

[42] N. Vandewalle, M. Ausloos, and P. Boveroux, Physica A **269**, 170 (1999).

[43] P. Grau-Carles, Physica A **287**, 396 (2000).

[44] M. Ausloos, Physica A **285**, 48 (2000).

[45] M. Ausloos and K. Ivanova, Physica A **286**, 353 (2000).

[46] M. Ausloos and K. Ivanova, Phys. Rev. E (to be published) (2001).

[47] M. Ausloos and K. Ivanova, Int J Mod Phys C (to be published) (2001).

[48] K. Ivanova and M. Ausloos, Physica A **274**, 349 (1999).

[49] A. Montanari, R. Rosso, and M. S. Taqqu, Water Resour. Res. **36**, (5) 1249 (2000).

[50] C. Matsoukas, S. Islam, and I. Rodriguez-Iturbe, J. Geophys. Res-Atmos. **105**, 29 (2000).

[51] B.D. Malamud and D.L. Turcotte, J. Stat. Plan. Infer. **80**, 173 (1999).

[52] C.L. Alados, M.A. Huffman, Ethology **106**, 105 (2000).

[53] C.-K. Peng, J.E. Mietus, J.M. Hausdorff, S. Havlin, H.E. Stanley, and A.L. Goldberger, Phys. Rev. Lett. **70**, 1343 (1993).

[54] N. Makarenko, L.M. Karimova, B.I. Demchenko and M.M. Novak, Fractals **6**, 359 (1998).

[55] G. M. Viswanathan, S. V. Buldyrev, E. K. Garger, V. A. Kashpur, L. S. Lucena, A. Shlyakhter, H.E. Stanley, and J. Tschiersch, Phys. Rev. E **62**, 4389 (2000).

[56] E. Koscielny-Bunde, A. Bunde, S. Havlin, H. E. Roman, Y. Goldreich, H. J. Schellnhuber, Phys. Rev. E **81**, 729 (1998).

[57] E. Koscielny-Bunde, H. E. Roman, A. Bunde, S. Havlin, and H. J. Schellnhuber, Philo. Mag. B **77**, 1331 (1998).

[58] K. Ivanova, M. Ausloos, E. E. Clothiaux, and T. P. Ackerman, Europhys. Lett. **52**, 40 (2000).

[59] P. Talkner and R. O. Weber, Phys. Rev. E **62**, 150 (2000).

[60] Y. Ogata, K. Abe, Int. Stat. Rev. **59**, 139 (1991).

[61] H.A. Makse, S. Havlin, M. Schwartz, and H.E. Stanley, Phys. Rev. E **53**, 5445-5449 Part B (1996).

[62] K. Hu, P.Ch. Ivanov, Z. Chen, P. Carpena and H.E. Stanley, Phys. Rev. E **64**, 011114 (2001).

[63] M.F. Shlesinger and G.H. Weiss, *The Wonderful world of stochastics : a tribute to Elliott W. Montroll*, (North-Holland, New York, 1985).

[64] D. Stauffer and H. E. Stanley, *From Newton to Mandelbrot*, Second edition, (Springer-Verlag, Berlin, 1996).

[65] R.L. Stratonovich, *Topics in the Theory of Random Noise Vol. 1* (Gordon & Breach, New York, 1981).

[66] A. Witt, J. Kurths, and A. Pikovsky, Phys. Rev. E **58**, 1800 (1998).

[67] C.-K. Peng, S.V. Buldyrev, A.L. Goldberger, S. Havlin, F. Sciortino, M. Simons, H.E. Stanley, Nature (London) **356**, 168 (1992).

[68] S.V. Buldyrev, N.V. Dokholyan, A.L. Goldberger, S. Havlin, C.-K. Peng, H.E. Stan and G.M. Viswanathan, Physica A **249**, 430 (1998).

[69] H.E. Stanley, S.V. Buldyrev, A.L. Goldberger, S. Havlin, C.-K. Peng and M. Simo Physica A **273**, 1 (1999).

[70] P.Ch. Ivanov, L.A. Nunes Amaral, A.L. Goldberger, S. Havlin, M.G. Rosenblu Z.R. Struzik, and H.E. Stanley, Nature (London) **399**, 461 (1999).

[71] Y. Ashkenazy, P.Ch. Ivanov, S. Havlin, C.-K. Peng, Y. Yamamoto, A.L. Goldberg and H.E. Stanley, Computers in Cardiology **27**, 139 (2000).

[72] P.Ch. Ivanov, L.A. Nunes Amaral, A.L. Goldberger, M.G. Rosenblum, H.E. Stan and Z.R. Struzik, Chaos **11**, 641 (2001).

[73] J.M. Hausdorff, C.-K. Peng, Z. Ladin, J. Wei and A.L. Goldberger, J. Applied Phys **78**, 349 (1995).

[74] S. Bahar, J.W. Kantelhardt, A. Neiman, H.H.A. Rego, D.F. Russell, L. Wilke A. Bunde, and F. Moss, Europhys. Lett. **56**, 454 (2001).

[75] P.Ch. Ivanov, L.A. Nunes Amaral, A.L. Goldberger, and H.E. Stanley, Europh Lett. **43**, 363 (1998).

[76] J.W. Kantelhardt, E. Koscielny-Bunde, H.H.A. Rego, S. Havlin, and A. Bunde, Ph ica A **294**, 441 (2001).

[77] M.A. Carskadon and W.C. Dement, *Principle and Practice of Sleep Medicine* (V Saunders Co., Philadelphia, 2000).

[78] D. J. Dijk, C. A. Czeisler, Neurosci. Lett. 166 (1994) 63.

[79] C. A. Czeisler, J. F. Duffy, T. L. Shanahan, E. N. Brown, J. F. Mitchell, D. W. Rimmer, J. M. Ronda, E. J. Silva, J. S. Allan, J. S. Emens, D. J. Dijk, R. E. Kronauer, Science 284 (1999) 2177.

[80] N. Kleitman, Sleep 5 (1982) 311.

[81] P. Lavie, Chronobiol. Int. 6 (1989) 21.

[82] S. M. Patterson, D. S. Krantz, L. C. Montgomery, P. A. Deuster, S. M. Hedges, L. E. Nebel, Psychophysiology 30 (1993) 296.

[83] N. Aoyagi, K. Ohashi, S. Tomono, Y. Yamamoto, Am. J. Physiol. Heart Circ. Physiol. 278 (2000) H1035.

[84] A. C. Leary, P. T. Donnan, T. M. MacDonald, M. B. Murphy, American Journal of Hypertension 13 (2000) 1067.

[85] G. Jean-Louis, M. V. Mendlowicz, J. C. Gillin, M. H. Rapaport, J. R. Kelsoe, F. Zizi, H. P. Landolt, H. Von Gizycki, Physiology & Behavior 70 (2000) 49.

[86] C. A. Czeisler, R. E. Kronauer, J. S. Allan, J. F. Duffy, M. E. Jewett, E. N. Brown, J. M. Ronda, Science 244 (1989) 1328.

[87] E. N. Brown, C. A. Czeisler, J. Biol. Rhythms 7 (1992) 177.

[88] B. D. Lewis, D. F. Kripke, D. M. Bowden, Physiology & Behavior 18 (1977) 283.

[89] Z. Chen, P. Ch. Ivanov, K. Hu, H. E. Stanley, Phys. Rev. E 65 (2002) 041107.

[90] G. Nagels, P. Marion, B. A. Pickut, L. Timmermans, P. P. DeDeyn, Electromyography and Motor control-electroencephalography and Clinical Neurophysiology 101, (1996) 226.

[91] J. M. Winters, G. Loeb, Biomechanics and Neural Control of Posture and Movement, edited by J. M. Winters, P. E. Crago, Springer Verlag, New York, 2000.

[92] J. M. Haudsdorff, C. K. Peng, Z. Ladin, J. Y. Wei, A. L. Goldberger, J. Appl. Phys. 78 (1995) 349.

[93] Y. Q. Chen, , M. Z. Ding, J. A. S. Kelso, Phys. Rev. Lett. 79 (1997) 4501.

[94] R. L. Sacco, B. Boden-Albala, R. Gan, X. Chen, D. E. Kargman, S. Shea, M. C. P. and W. A. Hauser, Stroke incidence among white, black, and Hispanic residents of urban community: the Northern Manhattan Stroke Study, Am. J. Epidemiol. 1 259—268 (1998).

[95] S. Schwarz, D. Georgiadis, A. Aschoff and S. Schwab, Effects of body position intracranial pressure and cerebral perfusion in patients with large hemispheric stro Stroke 33, 497—501 (2002).

[96] P. J. Eames, M. J. Blake, S. L. Dawson, R. B. Panerai and J. F. Potter, Dynai cerebral autoregulation and beat to beat blood pressure control are impaired in ac ischaemic stroke, J. Neurol Neurosur. Ps. 72, 467—473 (2002).

[97] L. A. Lipsitz, S. Mukai, J. Hammer, M. Gagnon and V. L. Babikian, Dynamic re lation of middle cerebral artery blood flow velocity in aging and hypertension, Str 31, 1897—1903 (2000).

[98] L. Cupini, M. Diomedi, F. Placidi, M. Silvestrini and P. Giacomini, Cerebrovascu reactivity and subcortical infarctions, Arch. Neurol 58, 577—581 (2001).

[99] V. Novak, J. M. Spies, P. Novak, B. R. McPhee and T. A. Rummans, Hypocap and cerebral hypoperfusion in orthostatic intolerance, Stroke 29, 1876—1881 (199

[100] J. M. Serrador, P. A. Picot, B. K. Rutt, J. K. Shoemaker and R. L. Bondar, MRI M sures of Middle Cerebral Artery Diameter on Conscious Humans During Simula Orthostasis, Stroke 31, 1672—1678 (2000).

[101] H. S. Markus and M. J. Harrison, Estimation of cerebrovascular reactivity using transcranial Doppler, including the use of breath holding as the vasodilatatory stimulus, *Stroke* **23**, 668—673 (1992).

[102] V. Novak, P. Novak and R. Schondorf, Accuracy of beat-to-beat noninvasive measurement of finger arterial pressure using the Finapres: a spectral analysis approach, *J. Clin. Monitor. Comp.* **10**, 118—126 (1994).

[103] J. F. Claerbout. *Fundamentals of Geophysical Data Processing* (McGraw-Hill, New York, 1997).

[104] S. L. Marple, Computing the discrete-time analytic signal via FFT, *IEEE T. Signal Proces.* **47**, 2600—2603 (1999).

[105] A. V. Oppenheim and R. W. Schafer, *Discrete-Time Signal Processing, 2nd edition* (Prentice-Hall, Upper Saddle River, New Jersey, 1998).

[106] M. G. Rosenblum, A. S. Pikovsky and J. Kurths, Phase synchronization of chaotic oscillators, *Phys. Rev. Lett.* **76**, 1804—1807 (1996).

[107] M. G. Rosenblum, A. S. Pikovsky and J. Kurths, From phase to lag synchronization in coupled chaotic oscillators, *Phys. Rev. Lett.* **78**, 4193—4196 (1997).